



UNIVERSITÀ DEGLI STUDI DI PADOVA

Dipartimento di Fisica e Astronomia “Galileo Galilei”

Corso di Laurea in Fisica

Tesi di Laurea

BEAM TEST WITH POSITRONS ON TARGET
FOR THE PRODUCTION
OF A LOW EMITTANCE MUON BEAM

Relatore:

Prof. MARCO ZANETTI

Università degli Studi di Padova

Laureanda:

ALTEA LORENZON

matr. 1103173

ANNO ACCADEMICO 2016-2017

Abstract

The use of muon beams in High Energy Physics experiments has become more and more interesting for different research branches, from rare decay searches to neutrino physics up to muon colliders feasibility studies. Thus the production of low emittance muon beams is a key issue: since with the traditional muon sources, like K/π decays, this cannot be achieved if not with complex and still object-of-study techniques, a novel approach has been proposed, using electron-positron collisions at centre-of-mass energy just above the $\mu^+\mu^-$ production threshold realized with a 45 GeV positron beam interacting with target. In order to verify the possibility to obtain *ab initio* a low emittance muon beam from positrons on target, a test beam at CERN has been proposed and recently completed, from 26th July 2017 to 2nd August 2017.

This work, after a brief introduction on muon colliders and sources in Chapter 1, focuses on the test beam realization: Monte Carlo simulations will be discussed in Chapter 2, as well as the experimental setup choice in Chapter 3 and some of the first data analysis results in Chapter 4.

Contents

List of Figures	vii
List of Tables	ix
1 Introduction: Muon Collider	1
1.1 Physics motivations	1
1.2 Muon sources	2
1.2.1 The traditional way: muons from K/π decays	2
1.2.2 A new proposal: muon pair production from e^+e^- annihilation	3
2 LEMMA Test Beam: Description	5
2.1 Main goals of the test	5
2.2 Processes at $\sqrt{s} \sim 0.212$ GeV	5
2.2.1 The process $e^+e^- \rightarrow \mu^+\mu^-$	6
2.2.2 The process $e^+e^- \rightarrow e^+e^-(\gamma)$	9
2.3 Experimental setup	10
2.3.1 Positron beam	10
2.3.2 Target requests	10
2.3.3 Layout of the experiment	11
2.4 Monte Carlo Simulations	13
2.4.1 Signal characterization	14
2.4.2 Background characterization	15
2.4.3 Search for correlation in $\mu^+\mu^-$ hits position	17
3 LEMMA Test Beam: Realization	23
3.1 Overview	23
3.2 Full description of the detectors	24
3.2.1 Muon Chamber	25
3.2.2 Silicon Detectors	26
3.2.3 Calorimeters	27
3.2.4 Scintillator Detectors	28

3.3 Trigger and data acquisition	28
4 Data Analysis and First Results	33
4.1 Tracking system: Silicon telescopes	33
4.2 Calorimetry	38
4.2.1 Calorimeters on the μ^- line	38
4.2.2 Calorimeters on the μ^+ line	38
4.2.3 Correlation studies in calorimeters	40
4.2.4 Energy-position relation in DEVA	43
4.3 Muon Chamber performances	45
4.3.1 Time boxes	46
4.3.2 Occupancies	46
4.3.3 Track reconstruction in the Muon Chamber	48
4.4 Event building and tagging	49
Conclusion	49
A Characteristics of runs analyzed	53
Bibliography	55

List of Figures

1.1	Schematic layouts of a muon collider	4
1.2	Preliminary scheme for low emittance muon beam production	4
2.1	Feynman diagram of muon pair production	6
2.2	Muon pair production cross section	7
2.3	Muon energy spread just above threshold	8
2.4	Muon scattering angle distribution	9
2.5	Feynman diagrams of Bhabha processes	9
2.6	Correlation of scattering angle and longitudinal energy in Bhabha process	10
2.7	Layout of the experiment in Monte Carlo simulations	12
2.8	Simulated $\mu^+\mu^-$ position and momentum on Muon Chamber	15
2.9	Simulated e^+e^- position and momentum on Muon Chamber	16
2.10	Simulated γ position and momentum on Muon Chamber	17
2.11	Simulated $\mu^+\mu^-$ hits distribution on Si40	18
2.12	Correlation between variables defined in (2.12) and (2.13)	19
2.13	Correlation between variables defined in (2.16) and (2.17)	20
2.14	Distribution of θ and ΔR for $\mu^+\mu^-$ correlation studies	21
3.1	The experimental area	23
3.2	Layout of the test beam experimental setup	24
3.3	Scheme of a drift tube from a DT Chamber	25
3.4	The mean-time principle	26
3.5	Insight view of DEVA calorimeter	27
3.6	Data acquisition crates	28
3.7	Muon chamber in H4	30
3.8	Silicon detectors in their final position	31
3.9	Pictures of the calorimeters	31
3.10	Scintillator detector	31
3.11	A screenshot of SPS Page One	32

4.1	Alignment of Si20 relative to Si10	34
4.2	Alignment of Si30 relative to Si10	35
4.3	Alignment of Si30 relative to Si20	35
4.4	Alignment of Si40 relative to Si10	36
4.5	Alignment of Si40 relative to Si20	36
4.6	Alignment of Si40 relative to Si30	37
4.7	Correlation in Si50 and Si55	37
4.8	Correlation in Si51 and Si56	37
4.9	Pb glass calorimeter energy spectrum	38
4.10	Cherenkov calorimeter energy spectrum	39
4.11	DEVA energy spectrum	39
4.12	Correlation in Cherenkov calorimeter channels	40
4.13	Correlation between Pb glass and Cherenkov (front) calorimeters	40
4.14	Correlation between Pb Glass and Cherenkov (back) calorimeters	41
4.15	Test of Pb Glass and Cherenkov correlation	41
4.16	Correlation between Pb Glass and DEVA calorimeters	42
4.17	Correlation between Cherenkov (front) and DEVA calorimeters	42
4.18	Correlation between Cherenkov (back) and DEVA calorimeters	42
4.19	Test of Pb Glass, Cherenkov and DEVA correlation	43
4.20	Energy and position relation in DEVA	44
4.21	Tracks projection on DEVA calorimeter	44
4.22	Results of energy-and-position-based cuts on DEVA spectrum.	45
4.23	Time boxes of DT chamber	47
4.24	Muon Chamber occupancy	47
4.25	Track reconstruction event dispaly	49

List of Tables

2.1	Properties of Beryllium	11
2.2	Parameters of GEANT4 simulations	14
2.3	Fitting parameters of functions represented in Figure 2.12	19
2.4	Fitting parameters of functions represented in Figure 2.13	20
4.1	Muon Chamber t_{trig} results	46
A.1	Characteristics of Run 4604	53
A.2	Characteristics of Run 4606	53
A.3	Characteristics of Run 4607	54
A.4	Characteristics of Run 4608	54
A.5	Characteristics of Run 4611	54

Chapter 1

Introduction: Muon Collider

1.1 Physics motivations

A **muon collider** is a new particle accelerator facility in its conceptual design stage that collides muon beams. Muon colliders certainly introduce new interesting possibilities in the High Energy Physics field. There are several components to the answer at the question: **why study a muon collider?**

- Like electrons, muons are leptons, and in the collider framework this has two important implications. First, colliding elementary particles implies a small physics background and total conservation of (E, p) . Second, the full energy of the projectile is available for exploring the production of new particles. This is in contrast to a proton collider where, due to the quark subsystem, background is clearly not negligible and only a small fraction of the proton's momentum is available.
- Muons are heavy, nearly 200 times heavier than electrons. As synchrotron radiation from a charged particle varies inversely as the fourth power of the mass, muons could eliminate a big problem that physicists face when accelerating electrons: in a circular accelerator, electrons emit light and lose energy as they go around the ring. This puts a limit on the maximum energy that electrons can reach in such a machine. Instead, with muons it is possible to use a conventional circular accelerator, since synchrotron radiation is negligible; a multi-TeV Muon Collider is thus feasible. Another advantage that comes from muons' mass is a large direct coupling to the Higgs boson: in fact, s-channel scalar Higgs production is greatly enhanced in a $\mu^+\mu^-$ collider (with respect to e^+e^-) as the coupling is proportional to the lepton mass. A high brilliance muon beam is necessary for a Higgs Factory and allows precision measurements in the Higgs sector [1].

- Muons eventually decay in:

$$\mu^- \rightarrow e^- \nu_\mu \bar{\nu}_e \quad \mu^+ \rightarrow e^+ \bar{\nu}_\mu \nu_e \quad (1.1)$$

A Muon Collider realization goes hand in hand with a Neutrino Factory development and it represents an opportunity for carrying on an outstanding neutrino physics program.

- Feasibility studies have demonstrated that the machine has many attractive features: it is compact and it can fit on existing sites [2].

However, there are still technical problems that must be solved. Since muons only last for about $2.2\ \mu s$ in their rest coordinate system, it is a challenge to produce and accelerate them before a significant loss through decay has occurred. Even major problems are caused by electrons produced from μ decay in a beam pipe: these electrons heat the superconducting magnets both through the direct showers they produce as well as the synchrotron radiation that they emit in the magnetic field; furthermore they represent a significative background in the interacting region. Finally, an important issue is the muon beam production, which will be discussed more in depth in the following Section 1.2.

1.2 Muon sources

1.2.1 The traditional way: muons from K/π decays

Muon beams are usually obtained via K or π decays:

$$K^+ \rightarrow \mu^+ + \nu_\mu \quad K^- \rightarrow \mu^- + \bar{\nu}_\mu \quad (1.2)$$

$$\pi^+ \rightarrow \mu^+ + \nu_\mu \quad \pi^- \rightarrow \mu^- + \bar{\nu}_\mu \quad (1.3)$$

K and π are at their turn obtained by proton interaction with targets.

Muons are therefore produced as tertiary particles in a process chain and thus present large spreads both in energy and angular ranges: the final state occupies a rather diffused area in position-and-momentum phase space or, more precisely, it has high **emittance**. So when produced they do not represent, *de facto*, a beam. To alleviate this problem one may use either new large aperture accelerators or try to reduce (“cool”) the incoming muon beam phase space. The cooling strategy reduces the transverse “hot” motion of the muons by slowing them down (the muon beam passes through a material in which it loses energy) and then accelerating them in forward direction through high field solenoid, high temperature super conductors and radio frequency cavities [3]. This process is repeated many times: the main consequence is a substantial loss of the muon beam.

Thus R&D in this field is required and currently underway [4].

1.2.2 A new proposal: muon pair production from e^+e^- annihilation

A novel approach, which is the basic idea of **LEMMA** (Low EMittance Muon Accelerator), involves electron-positron collisions:

$$e^+e^- \rightarrow \mu^+\mu^- \quad (1.4)$$

In particular these collisions are required to happen just above the $\mu^+\mu^-$ production threshold with maximal beam energy asymmetry: this implies using a positron beam of 45 GeV interacting with a target (as shown in Chapter 2).

Many advantages are provided by following this new approach: in fact, muon cooling would not be necessary, since the properties of muons produced by positrons on target are already those required for a beam. In particular low and tunable muon momentum in the rest frame and large Lorentz boost, about $\gamma \sim 200$. This has important consequences:

- muons produced just above threshold are highly collimated, since the final state has a small emittance;
- they have an average laboratory lifetime $\tau_\mu^{lab} \approx 500\ \mu s$, which allows further acceleration before the muons' decay: fast muon acceleration concepts are deeply studied by Muon Accelerator Program (MAP) at Fermilab [5].

In Figure 1.1 a comparison between a muon collider where muons are produced from K/π decays and where muons are produced by positrons on target is shown. The advantage of producing a highly collimated muon beam from the beginning, and thus to avoid a delicate step in the process, is evident, since design will be easier and cheaper.

However, there are still some difficulties to deal with. First of all, cross section of (1.4) just above threshold is very small, about $1\ \mu b$, with substantial repercussions on muon production rate. At the center of mass energy of $2m_\mu \simeq 0.212\text{ GeV}$ the dominant process is Bhabha scattering. Furthermore a small cross section also implies specific requests for the positron beam and the target's electron density, in order to compensate the extremely low muon production efficiency. Studies on these issues are currently underway.

A preliminary scheme for the low emittance muon beam production chain is shown in Figure 1.2. This project [7] is based on a “multipass scheme” with a positron storage ring to increase muon production efficiency with respect to a “single pass scheme”. In this scheme positrons are produced from e^- impinging on target, collected and then accelerated to be injected in a 6.3 km long storage ring with a target. Muons produced by this 45 GeV positron beam are then collected in two 60 m long high momentum Acceptance Rings, where they will be recombined in bunches,

for $\sim 1 \tau_\mu^{lab} \approx 2500$ turns.

In such a scheme, two main issues have to be understood and are currently being studied: first, e^+ rate production should amount to $10^{17} e^+/s$; second, the target positioned in the positron ring should support a dissipated power $\mathcal{O}(100 \text{ kW})$.

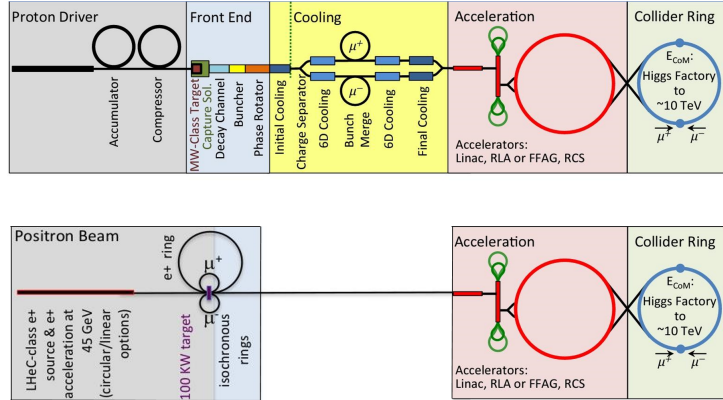


Figure 1.1: From [6], comparison between a muon collider layout that includes a muon ionization cooling facility and LEMMA layout.

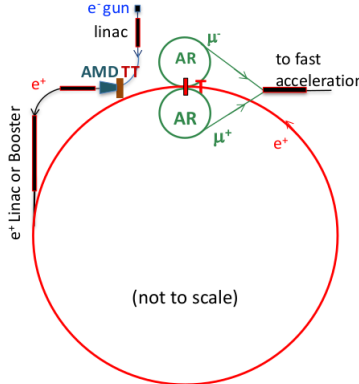


Figure 1.2: Preliminary scheme for a low emittance muon beam production.

In order to verify the possibility to obtain *ab initio* a low emittance muon beam from positrons on target a test beam at CERN has been proposed and recently completed. The description and the realization of the experimental work are presented in the following Chapter 2 and Chapter 3, while in Chapter 4 first results of data analysis are reported.

Chapter 2

LEMMA Test Beam: Description

2.1 Main goals of the test

One of the most interesting implications of LEMMA is the possibility to obtain a muon beam with low emittance and high values of brilliance, defined as the ratio of the intensity to the normalized emittance [8]. Monte Carlo simulations provide accurate predictions, but an experimental measurement of this key parameter is needed. LEMMA test beam has been proposed with these specific goals:

- To measure the $e^+e^- \rightarrow \mu^+\mu^-$ differential cross section at threshold, since it has never been done before.
- To measure the emittance of the outgoing muons: this is the key issue of the LEMMA proposal.

In order to achieve these results, it is crucial to identify particles after the target, to track muons back to the production vertex and to measure their momentum. Monte Carlo simulations have been done to find the best configuration of the experimental setup, described in Section 2.3.

With the same experimental setup it is also possible to carry out studies on positron beam degradation.

2.2 Processes at $\sqrt{s} \sim 0.212 \text{ GeV}$

The dominant processes at the muon production threshold energy are the following:

1. Muon pair production: $e^+e^- \rightarrow \mu^+\mu^-$;
2. Bhabha scattering: $e^+e^- \rightarrow e^+e^-(\gamma)$;

3. e bremsstrahlung;
4. $\gamma\gamma$ scattering: $e^+e^- \rightarrow \gamma\gamma$.

Due to the higher cross section, the second process represents the most significant source of noise for the case to be studied; the third one has instead a smaller yet well known cross section. This fact can be exploited, since the cross section is related to the number of events and the luminosity:

$$N_{\gamma\gamma} = L \cdot \sigma_{e^+e^- \rightarrow \gamma\gamma} \quad (2.1)$$

So by measuring $N_{\gamma\gamma}$ an estimation of L , and thus muon rate normalization, can be obtained.

Only the muon pair production process and the Bhabha scattering will be discussed in the following 2.2.1 and 2.2.2.

2.2.1 The process $e^+e^- \rightarrow \mu^+\mu^-$

Muon pair production from electron-positron annihilation is the basis of LEMMA proposal: in Figure 2.1 the Feynman diagram of this process is shown.

Thus it is a crucial point to study the dependencies that can maximize muon pair production and at the same time minimize the muon bunch emittance and energy spread. The main parameters that contribute at these goals are:

- the cross section on the centre of mass energy;
- the outcoming muon energy spread;
- the muon scattering angle distribution.

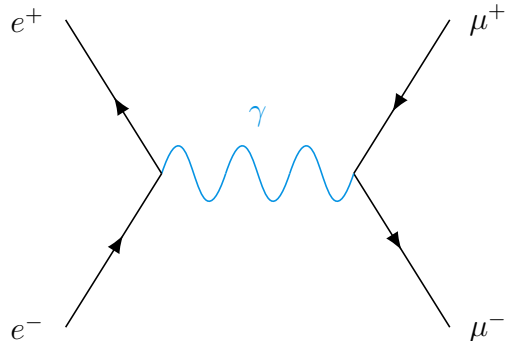


Figure 2.1: Feynman diagram of muon pair production from electron-positron annihilation.

Cross section at threshold The cross section for muon pair production just above threshold is shown in Figure 2.2. It's obtained using the Born cross section, enhanced by a factor called Sommerfeld-Schwinger-Sakarov (SSS) threshold Coulomb resummation factor [9]: the cross section of the process is enhanced just above threshold because of muonium bound states.

The cross section value reaches its maximum of $1 \mu\text{b}$ at $\sqrt{s} \sim 0.230 \text{ GeV}$: this is the value that has been taken into account for further studies.

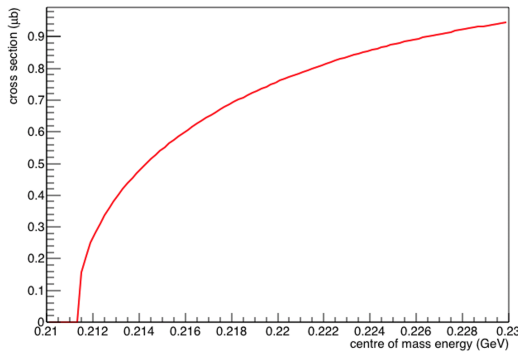


Figure 2.2: From [8], muon pair production cross section as function of centre-of-mass-energy.

Energy spread The energy spread of the outgoing muons depends on the centre-of-mass energy available for the collision. In particular it is possible to calculate:

$$E_\mu^{\max} = \gamma (E_\mu^* + \beta p_\mu^*) \quad (2.2)$$

$$E_\mu^{\min} = \gamma (E_\mu^* - \beta p_\mu^*) \quad (2.3)$$

where $E_\mu^* = \sqrt{s}/2$ is the muons' energy in the rest frame and $p_\mu^* = \sqrt{\frac{s}{4} - m_\mu^2}$ their momentum in the same frame.

In the approximation

$$\gamma = \frac{E_{e^+}}{\sqrt{s}} = \frac{\frac{s}{2m_e} - m_e}{\sqrt{s}} \approx \frac{\sqrt{s}}{2m_e} \quad (2.4)$$

and $\beta = 1$, equations (2.2) and (2.3) become

$$E_\mu^{\max} = \frac{\sqrt{s}}{2m_e} \left(\frac{\sqrt{s}}{2} + \sqrt{\frac{s}{4} - m_\mu^2} \right) \quad (2.5)$$

$$E_\mu^{\min} = \frac{\sqrt{s}}{2m_e} \left(\frac{\sqrt{s}}{2} - \sqrt{\frac{s}{4} - m_\mu^2} \right) \quad (2.6)$$

Figure 2.3 shows muon energy distribution E_μ^{max} and E_μ^{min} as a function of the center-of-mass energy.

Given the value of $\sqrt{s} = 0.230 \text{ GeV}$, according to (2.4) the Lorentz boost is $\gamma \approx 220$ and muons' energy varies between $E_\mu^{min} \approx 18 \text{ GeV}$ and $E_\mu^{max} \approx 26 \text{ GeV}$. As a consequence, the outcoming muons' momentum varies between $p_\mu^{min} \approx 18 \text{ GeV}/c$ and $p_\mu^{max} \approx 26 \text{ GeV}/c$.

These results are confirmed by Monte Carlo simulations, as shown in Section 2.4.

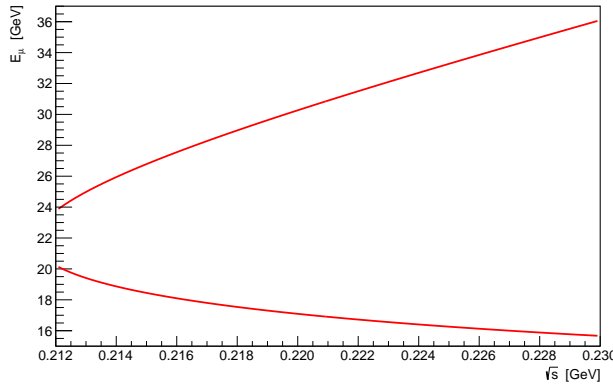


Figure 2.3: Muon energy distribution as function of centre-of-mass energy \sqrt{s} of the e^+e^- collisions.

Angular distribution The scattering angle of the outcoming muons θ_μ is maximum when muons are emitted orthogonally to the positron beam direction in the rest frame, and its value depends on \sqrt{s} :

$$\tan \theta_\mu^{max} = \frac{p_\mu^*}{\beta \gamma E_\mu^*} \quad (2.7)$$

With the approximations $\beta = 1$, $\tan \theta_\mu^{max} \sim \theta_\mu^{max}$ and (2.4), equation (2.7) becomes:

$$\theta_\mu^{max} = \frac{4m_e}{s} \sqrt{\frac{s}{4} - m_\mu^2} \quad (2.8)$$

Figure 2.4 shows the dependency of the variable θ_μ as a function of the centre-of-mass energy \sqrt{s} : muons produced with a very small momentum in the rest frame are contained in a cone whose size is increasing with energy.

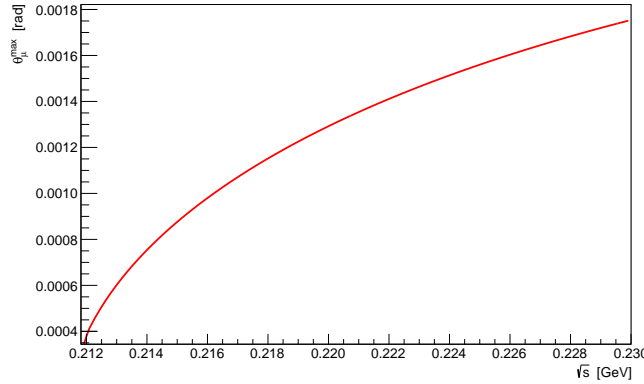


Figure 2.4: Muon scattering angle distribution as a function of centre-of-mass energy \sqrt{s} of the e^+e^- collisions.

2.2.2 The process $e^+e^- \rightarrow e^+e^-(\gamma)$

Bhabha scattering is the electron-positron scattering process $e^+e^- \rightarrow e^+e^-$. There are two leading-order Feynman diagrams contributing to this interaction: an annihilation process and a scattering process, both of them shown in Figure 2.5.

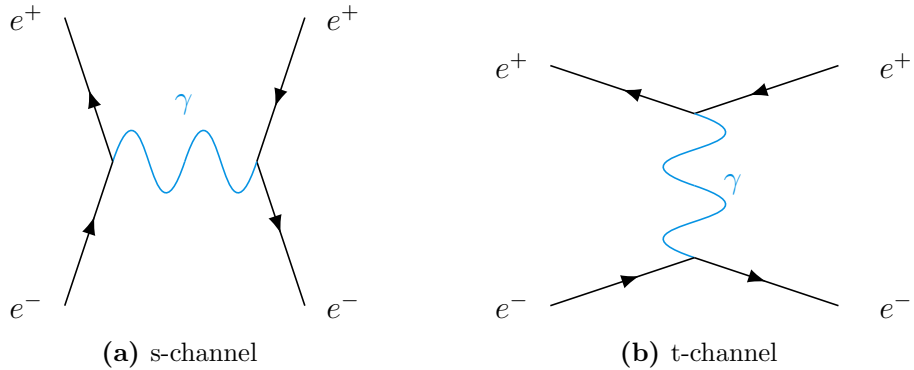


Figure 2.5: Feynman diagrams of s-channel Bhabha process (annihilation) (a), and t-channel (scattering) (b).

The process proceeds mostly via t-channel: positrons are produced with a very small scattering angle. The differential cross section of the process is proportional to $1/\sin^4 \theta$; so for small angles, at the considered energy of $\sqrt{s} \sim 0.212 \text{ GeV}$, it's ~ 5 order of magnitudes higher than that of muon pair production. However, at small scattering angles correspond higher values of longitudinal energy (as shown in Figure 2.6) than those of $\mu^+\mu^-$ produced at threshold (see 2.2.1). Bhabha events kinematically similar to $\mu^+\mu^-$ events are instead produced at higher scattering angle:

in this case the cross section is $\sim 1.88 \mu\text{b}$ and is comparable to muon pair production cross section.

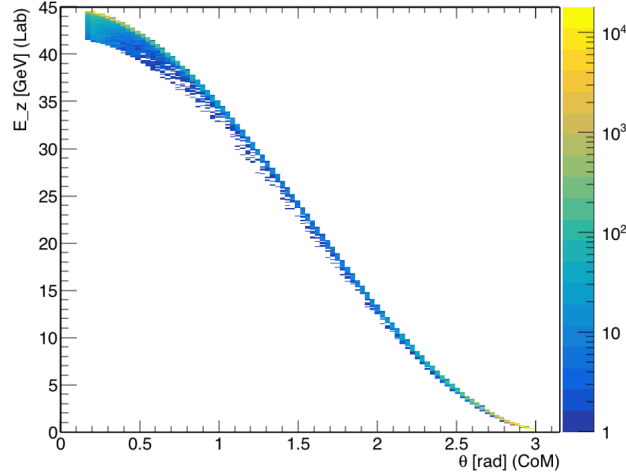


Figure 2.6: From [10], correlation of scattering angle and longitudinal energy in simulated Bhabha processes at $\sqrt{s} \sim 0.212 \text{ GeV}$.

Bhabha scattering represents the largest source of beam loss in this case, setting an upper limit on the muon pair production from positrons on target.

2.3 Experimental setup

2.3.1 Positron beam

With the center-of-mass energy of \sqrt{s} , the positron beam impinging on a fixed target has an energy given by the following:

$$E_{e^+} = \frac{s}{2m_e} - m_e \quad (2.9)$$

A value of $\sqrt{s} = 0.230 \text{ GeV}$ corresponds to $E_{e^+} \approx 45 \text{ GeV}$.

Since the final muon emittance also depends on the initial incoming beam emittance, the request for the positrons beam energy spread is quite compelling: 1% is the optimal value for this parameter. The purity of the incoming beam is required to be close to 99%.

2.3.2 Target requests

The choice of the target is also a key issue of the LEMMA proposal. Studies have been done [8] with the following criteria guiding the choice:

- the maximization of the number of μ pairs produced;
- the minimization of the outgoing muon beam emittance;
- the largest positrons survival, if needed for the positrons recirculation.

Two of the target's parameters that have been taken into account are the thickness of the target and the electron density of the material. For the test beam a 3 cm thick target of Beryllium has been chosen in order to maximize muon pair production; the main characteristics of the material are reported in Table 2.1.

Z	4
A	9.01214
X_0 (cm)	35.2
ρ (g/cm ²)	1.85

Table 2.1: Relevant properties of Beryllium.

The target thickness l and the electronic density ρ_{e^-} as well as the cross section $\sigma_{e^+e^- \rightarrow \mu^+\mu^-}$ and the number of positrons per spill n_{e^+} contribute to determine the number of muons produced in this way:

$$n_{\mu^+\mu^-} = n_{e^+} \rho_{e^-} l \sigma_{e^+e^- \rightarrow \mu^+\mu^-} \quad (2.10)$$

where the electronic density can be calculated:

$$\rho_{e^-} = \frac{Z}{A} N_A \rho \quad (2.11)$$

being Z the atomic number, A the mass number, N_A the Avogadro constant and ρ the material density.

However, this doesn't constitute a prototype target for the final configuration scheme (see 1.2.2).

2.3.3 Layout of the experiment

In order to achieve the experiment goals, tracking and identifying particles produced in the collisions of positron beam with target is fundamental. To satisfy this need the experimental setup consists of several detectors and a magnetic dipole: a layout of the experiment is displayed in Figure 2.7.

The components of the experimental setup at project level are:

- **Muon Chamber.** A Drift Tubes chamber from the CMS experiment provides muon identification and track reconstruction; the detector is also self-triggering.

- **Silicon detectors.** The Silicon telescopes close to the target are used to measure with high precision the incoming positron and the outgoing muon pair; the four Silicon detectors after the dipole are also used to track muons, allowing a measurement of the muon transverse phase space distribution.
- **Calorimeters.** Two calorimeters positioned in front of the Muon Chamber are used to measure the beam positrons and the emitted photons. Finally, a sampling calorimeter is necessary to distinguish Bhabha electrons from negative muons that constitute the signal $e^+e^- \rightarrow \mu^+\mu^-$ events.
- **Magnetic Field.** A magnetic field after the target is necessary to separate opposite-charged particles produced after the target and measure their momenta.
- **Absorber.** Since the magnetic field bends charged particles, the residuate positrons of the beam are deviated towards the chamber. To protect this detector from excessive radiation, a thick iron absorber is interposed on the beam line. At the same time the absorber also intercepts the μ^+ line: for this reason the positive muons' measurements will suffer from the multiple scattering effect. The μ^- line is instead left uncovered, allowing high precision measurements.

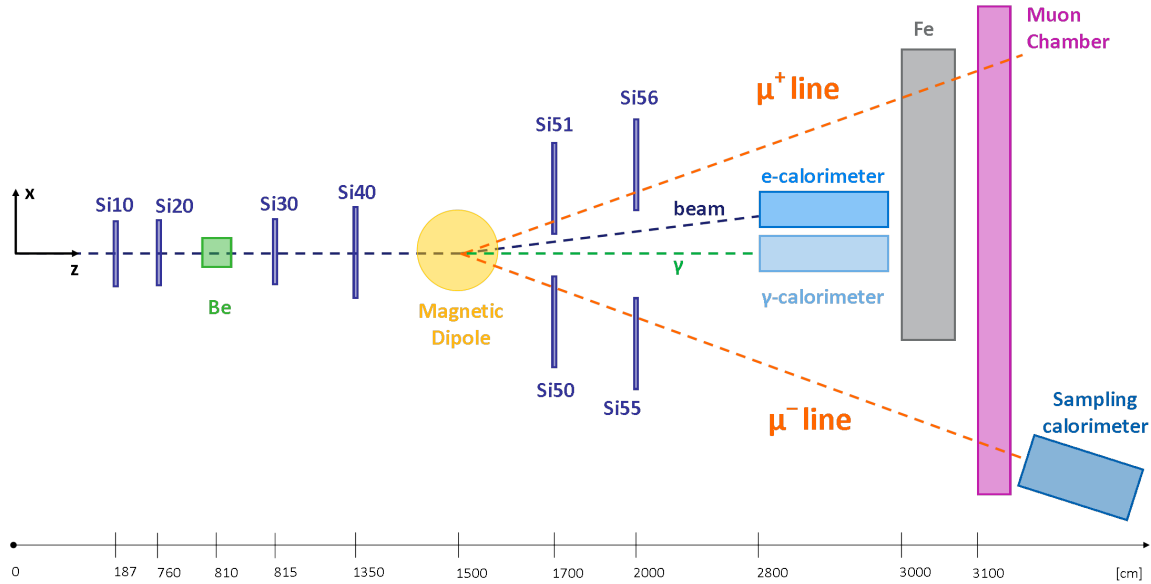


Figure 2.7: Layout of the test beam at project level, also used for Monte Carlo simulations (not to scale).

Signal $e^+e^- \rightarrow \mu^+\mu^-$ events are selected at the trigger level by means of the Muon Chamber and the sampling calorimeter recognizing the μ^- candidate as a MIP (Minimum Ionizing Particle). It has been demonstrated that after the muon identification provided by the Muon Chamber, the muon track segments can be extrapolated back and successfully associated with the silicon-detectors hits, allowing a complete track reconstruction.

2.4 Monte Carlo Simulations

Monte Carlo simulations have been performed using GEANT4 [11]. The experimental setup is the same shown in Figure 2.7. In these preliminary simulations detectors have been constructed as much as possible similar to the real ones. In fact they have the same dimensions (see Chapter 3) and also the material is simulated, except for the Muon Chamber, which is simply an empty volume. The target is a $5 \times 5 \times 3 \text{ cm}^3$ Beryllium crystal. Different dimensions and positions have been simulated for the absorber: in the final configuration it is a $2 \times 1 \times 0.5 \text{ m}^3$ iron block covering most of the Muon Chamber. The simulated magnetic dipole is a 40 cm long cylinder which produces a magnetic field measuring 1.26 T and oriented according to the y-axis in Figure 2.7. In order to reproduce the expected experimental conditions, the simulated environment has been filled with air.

The physics list for the **signal simulations**, i.e. the list of all physical processes that the software simulates, has been written *ad hoc* and comprehends:

- muon pair production from e^+e^- annihilation;
- multiple scattering for charged particles;
- Compton scattering;
- Bremsstrahlung for e and μ ;
- photo-electric effect;
- ionization and delta rays production;
- e^+ annihilation into photons and into hadrons;
- gamma conversion into e^+e^- and $\mu^+\mu^-$ couples.

Instead, for the **background simulations** the default ATLAS physics list, called FTFP_BERT [12], has been chosen.

Every simulated event corresponds to a positron on target.

Other parameters of the simulations are reported in Table 2.2. Cross section of muon pair production has been enhanced for computational reasons.

Number of events simulated	10^6
Beam composition	Positrons 100%
Beam energy	45 GeV
Beam section	$20 \times 20 \text{ mm}^2$ uniform distribution
Beam spread	$1.2 \cdot 10^{-4} \text{ rad}$
$\sigma_{e^+e^- \rightarrow \mu^+\mu^-}$ enhancement factor	10^3

Table 2.2: Parameters of the GEANT4 simulations for LEMMA test beam.

In the following paragraphs the main features of the $\mu^+\mu^-$ signal are investigated, as well as the background signal produced by electrons, positrons and photons.

2.4.1 Signal characterization

According to the GEANT4 simulation, different kind of particles are expected to arrive on the Muon Chamber's surface: muons, photons, electrons and positrons. The passage of these particles through the active volume of the Muon Chamber can lead to ionization, so it is necessary to distinguish which events correspond to the interesting process and which don't.

Events tagged as **signal** are characterized by a couple of muons hitting the Muon Chamber symmetrically with respect to the beam direction. In Figure 2.8 the position and the momentum of muons produced from e^+e^- annihilation is shown. As predicted in (2.2.1) muons momentum is distributed between 18 GeV and 26 GeV: the passage of these particles through the magnetic field allows to separate them according to their momentum and to find them in a specific region of the Muon Chamber: $-650 \text{ mm} \lesssim x_{\mu^-} \lesssim -450 \text{ mm}$ and $+450 \text{ mm} \lesssim x_{\mu^-} \lesssim +650 \text{ mm}$, while in the y-view the beam is well collimated. Once individuated the region where the μ^- hits are expected, the setting of the iron absorber is chosen accordingly: the border of the iron block will coincide with $x = -375 \text{ mm}$ in the Muon Chamber local reference frame. This choice allows to minimize the photons rate on the μ^- region, as shown also in Figure 2.10. The simulations also confirm that the correlation between muon momentum and hits position on the Muon Chamber is well defined.

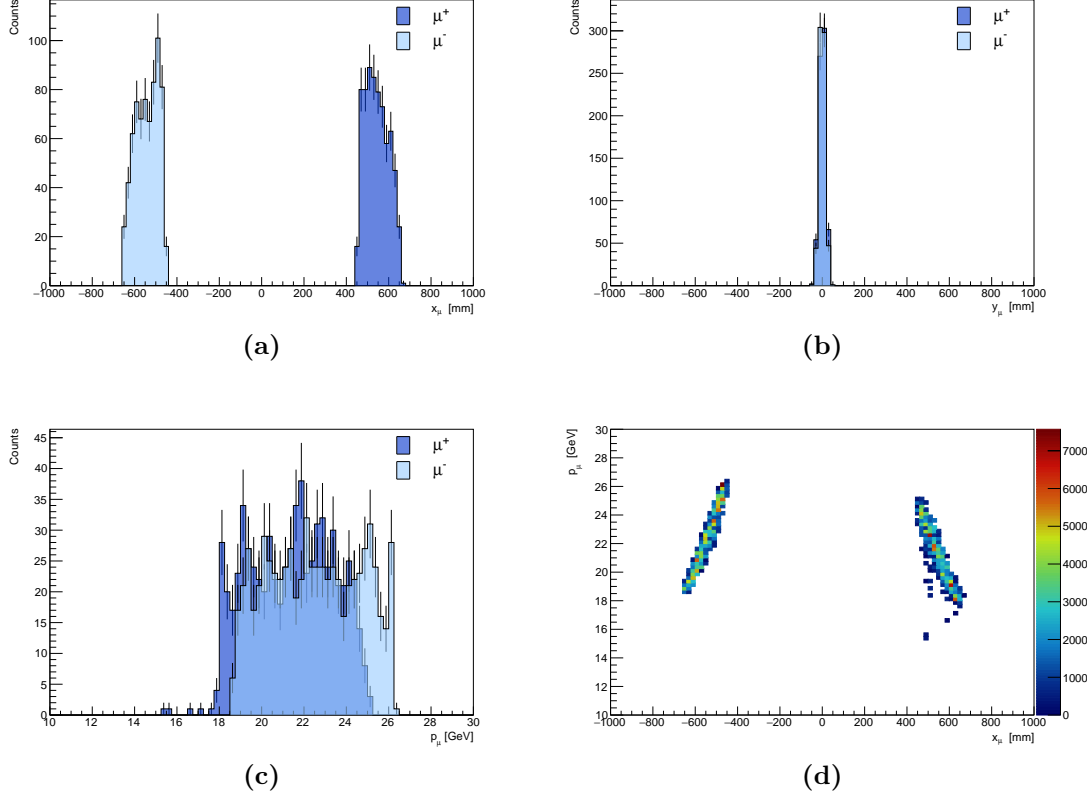


Figure 2.8: x-view (a) and y-view (b) of muon hits distribution on the Muon Chamber in the local reference frame; momentum distribution of the produced muon couple on the same detector (c); correlation between position and momentum of the muon couple (d).

2.4.2 Background characterization

The **background** signal is mainly composed by positrons and electrons. However, a high energy electron or positron impinging on the Muon Chamber Aluminium vessel will produce a shower, so the signal is quite different from the one left by a muon (3.2.1); furthermore, the calorimeters will help to distinguish the two kind of leptons.

Figure 2.9 displays the position and momentum of electrons and positrons impinging on the Muon Chamber surface: the edges of the iron absorber are clearly visible, both in the x-view and in the y-view (in particular from e^- produced in target); the simulation also confirms that with a 0.5 m thick iron block the Muon Chamber is well shielded from the direct beam positrons. Almost the totality of electrons and positrons impinging on this detector are produced by the beam positrons showering inside the absorber: the excess of electrons is explained considering that positrons

annihilate in matter, as justified by the spike at $p_\gamma \approx 0.5$ MeV in Figure 2.10. Electrons and positrons produced in the target (from s-channel Bhabha events) are highlighted. As expected only e^- survive and reach the Muon Chamber. Although the majority is concentrated in the same xz-plane of the beam, some of them appear as distributed on all the chamber surface because they loose a great part of their energy along their trajectory and suffer the multiple scattering effect. In the spectrum of e^- momentum a discontinuity is observed at $p_e \approx 12$ GeV, due to Bhabha electrons.

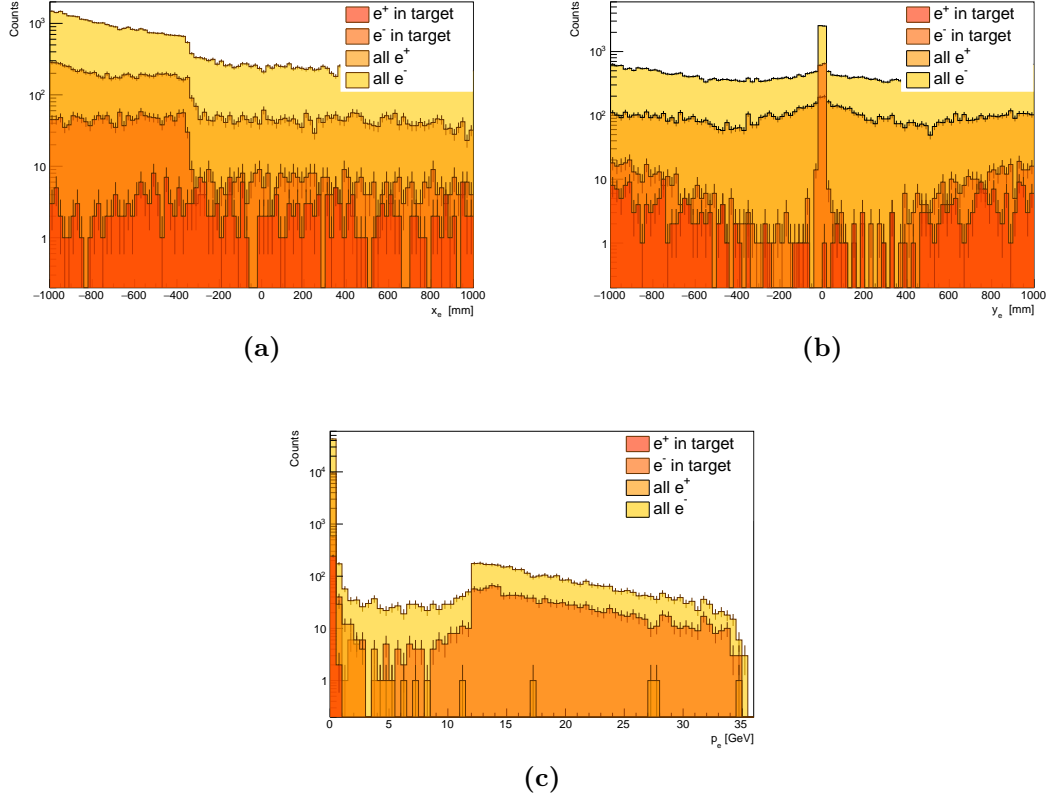


Figure 2.9: x-view (a) and y-view (b) of e^+e^- hits distribution on the Muon Chamber in the local reference frame; momentum distribution of these particles on the same detector (c). Different colours highlight the particles produced in target, coming from the s-channel Bhabha events.

Photons are produced mainly by bremsstrahlung and in electromagnetic showers inside the iron absorber. Figure 2.10 shows photon hit position distribution on the Muon Chamber surface and their momentum. The great part is concentrated in the extreme left region: all those photons come from electrons and positrons interacting with matter in the corner of the iron absorber, as well as the ones forming the small

spot in the central region. The momentum spectrum is quite smooth: the spike at $p_\gamma = m_e = 0.511 \text{ MeV}$ due to e^+e^- annihilation is clearly visible.

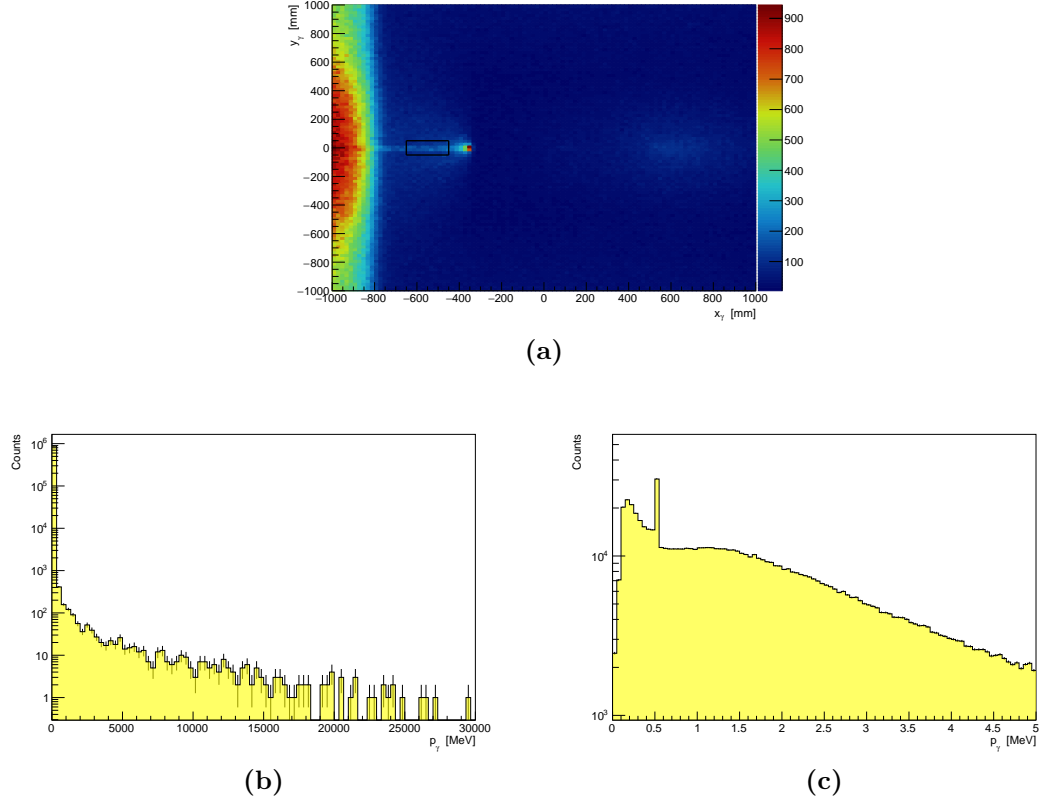


Figure 2.10: xy-plane view (a) of photon hits distribution on the Muon Chamber in the local reference frame and their momentum distribution on the same detector in the range 0 – 30 GeV (b) and 0 – 5 MeV (c).

2.4.3 Search for correlation in $\mu^+\mu^-$ hits position

Since μ^+ have to cross the iron absorber, extrapolating the tracks from the Muon Chamber back to the Silicon telescopes is quite difficult, because of the worse resolution on μ^+ track in the Muon Chamber. However, position and angular correlation between muon hits, which are produced back to back in the rest frame, is confirmed by Monte Carlo simulations. Thus it is possible to exploit this correlation to identify which of the hits on the Silicon telescopes is the one of μ^+ .

The study of $\mu^+\mu^-$ correlation has been made in particular for hits in the first Silicon detector before the magnetic dipole, Si40. The expected situation on Si40 is shown in Figure 2.11.

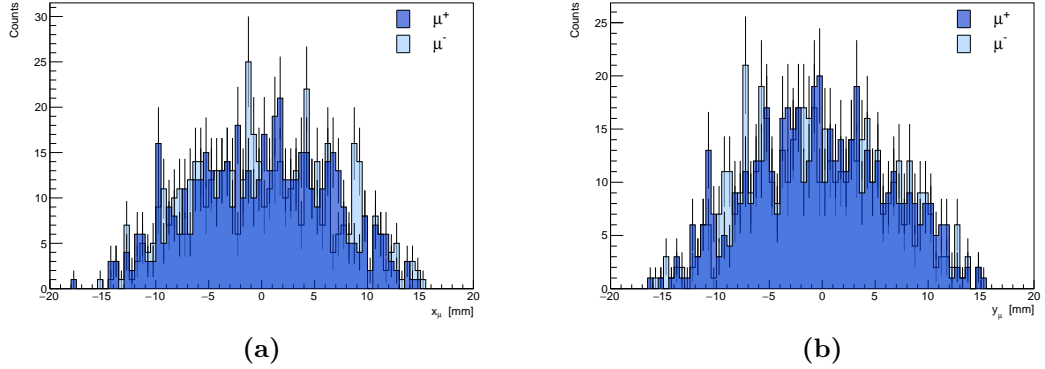


Figure 2.11: x-view (a) and y-view (b) of muon hits distribution on Si40 in the local reference frame.

Since the angular smearing of the impinging particles momentum is small, as shown in Table 2.2, in a first approximation the only component of the momentum considered not null is the one in the beam direction:

$$\vec{p} = (0, 0, p_z)$$

The defined variables for this study are the following:

$$X_{\mu^\pm} = x h_{\mu^\pm} - x v_{\mu^\pm} \quad (2.12)$$

$$Y_{\mu^\pm} = y h_{\mu^\pm} - y v_{\mu^\pm} \quad (2.13)$$

$$\theta = \left| \tan^{-1} \left(\frac{Y_{\mu^-}}{X_{\mu^-}} \right) - \tan^{-1} \left(\frac{Y_{\mu^+}}{X_{\mu^+}} \right) \right| \quad (2.14)$$

$$\Delta R = \sqrt{X_{\mu^-}^2 + Y_{\mu^-}^2} - \sqrt{X_{\mu^+}^2 + Y_{\mu^+}^2} \quad (2.15)$$

being $(xh_{\mu^\pm}, yh_{\mu^\pm})$ the muons hits' coordinates on Si40 and $(xv_{\mu^\pm}, yv_{\mu^\pm})$ the projection of their production vertex on the detector plane in the boost direction. It is expected:

$$\begin{array}{ll} X_{\mu^+} = -X_{\mu^-} & \theta = \pi \\ Y_{\mu^+} = -Y_{\mu^-} & \Delta R = 0 \end{array}$$

Figure 2.12 shows the dependency of the variables X_{μ^+} and Y_{μ^+} from X_{μ^-} and Y_{μ^+} respectively. As expected the trend of the distribution is linear: the function that fits the distribution is highlighted in black; its parameters are reported in Table 2.3.

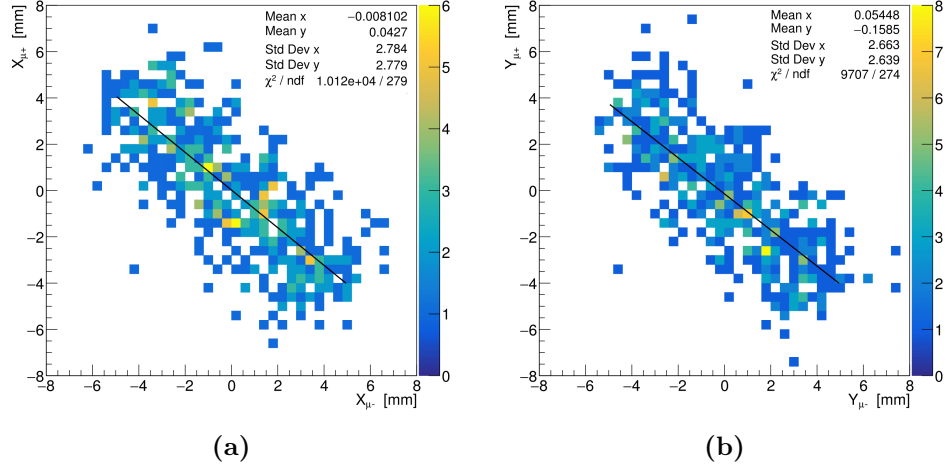


Figure 2.12: (a) Distribution of X_{μ^+} as a function of X_{μ^-} ; (b) Distribution of Y_{μ^+} as a function of Y_{μ^-} .

Function	a [mm]	b	Correlation Coefficient
$X_{\mu^+} = a + b \cdot X_{\mu^-}$	0.02 ± 0.11	-0.813 ± 0.043	-0.76
$Y_{\mu^+} = a + b \cdot Y_{\mu^-}$	-0.15 ± 0.11	-0.780 ± 0.041	-0.75

Table 2.3: Fitting parameters of functions represented in Figure 2.12.

θ and ΔR distributions are shown in Figure 2.14.

Further improvements have been done considering also the other momentum components of the impinging positrons and applying a correction in Lorentz boost direction: in order to find out a symmetry between muon coordinates the detector surface has to be rotated orthogonally to the positron direction. The variables (2.12) and (2.13) have to be redefined as follows, while (2.14) and (2.15) stay invariate:

$$X_{\mu^\pm} = x h'_{\mu^\pm} - x v_{\mu^\pm} \quad (2.16)$$

$$Y_{\mu^\pm} = y h'_{\mu^\pm} - y v_{\mu^\pm} \quad (2.17)$$

being $(x h'_{\mu^\pm}, y h'_{\mu^\pm})$ the muon hits coordinates in the rotated detector surface and $(x v_{\mu^\pm}, y v_{\mu^\pm})$ the projection of their production vertex on the detector plane in the boost direction. Again, it is expected

$$\begin{aligned} X_{\mu^+} &= -X_{\mu^-} & \theta &= \pi \\ Y_{\mu^+} &= -Y_{\mu^-} & \Delta R &= 0 \end{aligned}$$

Figure 2.13 shows the dependency of the variables X_{μ^+} and Y_{μ^+} from X_{μ^-} and Y_{μ^-} respectively. As expected the trend of the distribution is linear: the function that fits the distribution is highlighted in black; its parameters are reported in Table 2.4.

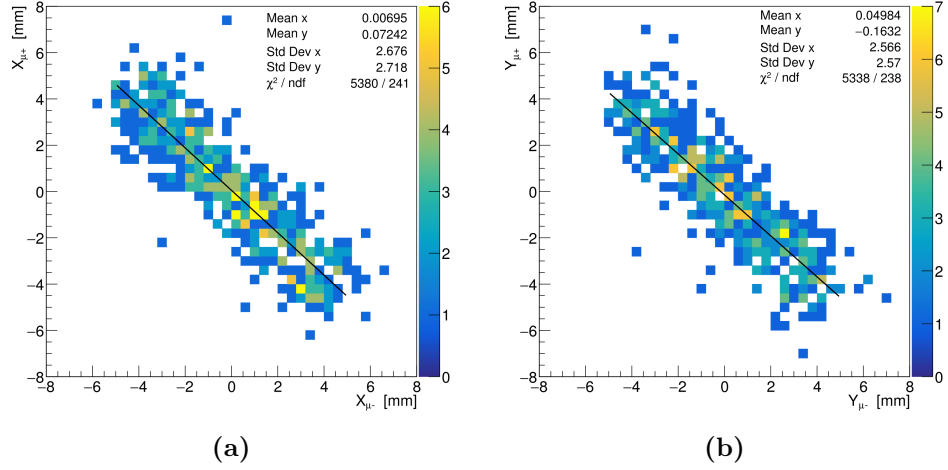


Figure 2.13: (a) Distribution of X_{μ^+} as a function of X_{μ^-} ; (b) Distribution of Y_{μ^+} as a function of Y_{μ^-} .

Function	a [mm]	b	Correlation Coefficient
$X_{\mu^+} = a + b \cdot X_{\mu^-}$	0.052 ± 0.084	-0.916 ± 0.032	-0.88
$Y_{\mu^+} = a + b \cdot Y_{\mu^-}$	-0.146 ± 0.083	-0.885 ± 0.033	-0.87

Table 2.4: Fitting parameters of functions represented in Figure 2.13.

In comparison with the distributions in Figure 2.12, those displayed in Figure 2.13 have a smaller standard deviation and show stronger correlation.

θ and ΔR distributions are shown in Figure 2.14. Both the histograms are more peaked around the expected values in case the correct boost direction is used with respect to the case in which the approximation of boost only in z direction is applied.

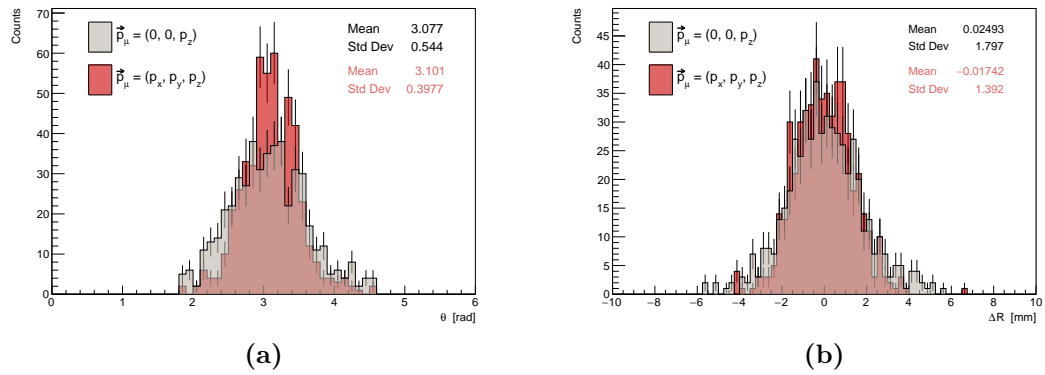


Figure 2.14: Distribution of variables defined by equations (2.14) (2.15) for muon correlation studies: θ (a), ΔR (b). Both cases, with Lorentz boost approximation (grey) and with the correct Lorentz boost direction (red), are presented.

Chapter 3

LEMMA Test Beam: Realization

3.1 Overview

LEMMA test beam has been realized at CERN with beam provided by the Super Proton Synchrotron in the H4 line, in the North Area (also shown in Figure 3.1). It started on 26th July 2017 and ended on 2nd August 2017, for a total of 7 days dedicated to setup preparation, calibration and data taking.

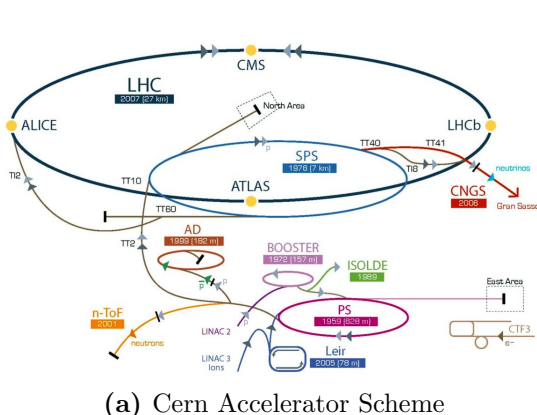


Figure 3.1: The experimental area: SPS fires protons towards North Area (a), converted in a positron beam for the H4 line where the test beam took place (b).

The final experimental setup is shown in Figure 3.2; a full description of all the detectors is presented in the following Section 3.2.

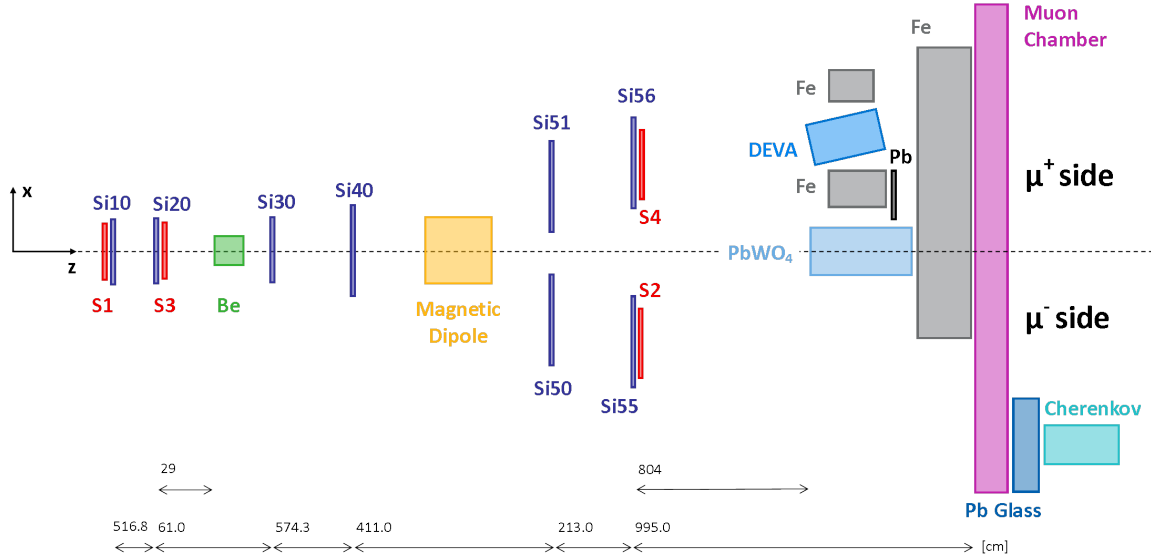


Figure 3.2: Final layout of the test beam experimental setup (not to scale). Some changes from the setup shown in Figure 2.7 have been made.

In order to align detectors a muon beam of 22.5 GeV was asked: such a beam can be produced from proton-on-target interactions and K/π decays as mentioned in Section 1.2. But the closeness of the experimental setup to the target has not allowed the alignment procedures: in fact, the muon beam received was too contaminated with pions to be suitable to the purpose. So the alignment strategy has proceeded with positron beam of different energies, also useful for detector calibration: 18 GeV, 22 GeV and 26 GeV.

Subsequently, data taking runs have begun, with a 45 GeV positrons beam: SPS could provide up to 4 spills/minute, and $5 \cdot 10^6$ positrons/spill; the spill duration was 4.8 s. With such a beam, the number of $\mu^+\mu^-$ signal events expected per spill is, with reference to relation (2.10), $n_{\mu^+\mu^-} \sim 7$ events/spill, which means up to $2.8 \cdot 10^5$ events in one week of uninterrupted data taking.

3.2 Full description of the detectors

In this Section the main features of the detectors used for LEMMA test beam are presented. Some of the following detectors are not part of the original project but their use has become necessary during the test beam, in particular the scintillator detectors.

3.2.1 Muon Chamber

The Drift Tubes chambers [13] are used in the CMS experiment to track muons in the central barrel. The basic detection unit is the drift cell, represented in Figure 3.3, which consists of an aluminum tube with a $42 \times 13 \text{ mm}^2$ section. The electric field is generated by an anode wire in the middle of the cell and two cathode strips on the shorter sides. To better shape the field lines around the anode two strips are added in correspondence to the wire. The electrodes are kept at high voltage: $V_{\text{wire}} = 3600 \text{ V}$, $V_{\text{strips}} = 1800 \text{ V}$ and $V_{\text{cathodes}} = 1200 \text{ V}$. The gas inside the cell is a mixture of Ar (85%) and CO₂ (15%). The choice of both the electrodes high voltage and the gas mixture has been made so that the drift velocity could be as much as possible constant: it results $v_{\text{drift}} = 54 \text{ cm}/\mu\text{s}$.

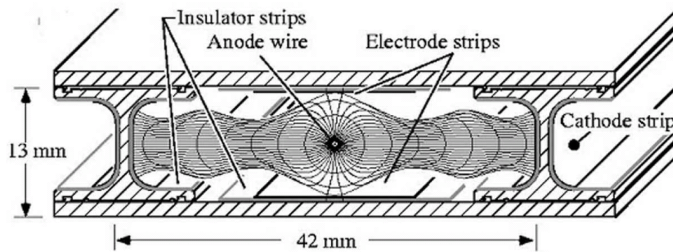


Figure 3.3: Scheme of a drift tube from a DT Chamber.

The cells are assembled into a rigid aluminium structure to form a DT chamber. The DT chambers have different size depending on their position inside the CMS experiment: the one employed for LEMMA test beam is a MB2, so it measures $245 \times 253 \times 29 \text{ cm}^3$. The cells are arranged to form three groups called super-layers (SL), each of them formed by four layers of cells: the layers inside a SL are staggered by half cell for triggering and hit reconstruction purposes. In a MB2 there are three SLs: two of them, the first one and the third, called $\phi - \text{SL}$, have wires running in parallel, while the second, called $\theta - \text{SL}$, is rotated by 90° with respect to the other two. A 128 mm thick Aluminium plate with a honeycomb structure is added to gather rigidity and to increase the level arm of the two $\phi - \text{SLs}$. For LEMMA test beam the DT chamber has been placed with vertical $\phi - \text{SLs}$ with respect to the ground in order to have better measurements in the bending plane.

Installed on the honeycomb plate there is an alluminium structure called “minicrate”, where first level of the read-out and trigger electronics of the DT are allocated. The read-out system is basically composed of Read Out Boards (ROB) and Read Out Servers (ROS). For the test beam a ROS with eight input channels (thus eight ROBs) has been used; each ROB contains four 32-channels TDC (Time to Digital Converter).

One of the main feature of the DT chambers is the triggering capability, performed by front-end devices called Bunch and Track Identifiers (BTI). The trigger mechanism is based on the following relation (“mean-time”), also illustrated in Figure 3.4:

$$T_{max} = t_2 + \frac{t_1 + t_3}{2} \quad (3.1)$$

being t_1, t_2, t_3 the raw times on three consecutive layers and T_{max} the maximum drift time, defined as $T_{max} = 2.1 \text{ cm}/v_{drift}$. The signals originated by a muon produce an “aligned” pattern after a time corresponding to T_{max} .

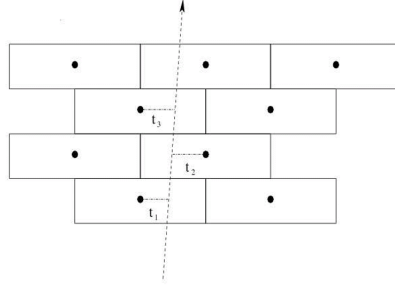


Figure 3.4: Example of drift times of a track satisfying the mean-time equation (3.1).

With a sampling frequency of 80 MHz, the BTIs look for such an alignment by comparing the drift times by means of a set of equations analogous to (3.1) and assign a quality flag on the track based on the number of hits (“H” corresponds to 4 hits, “L” corresponds to 3). Candidates are selected independently in the ϕ – SLs and in the θ – SL, but in the ϕ -view the BTI data undergo two further steps of processing: in the first step, the Track Correlator (TRACO) devices are used to correlate tracks in the two SL; in the second step the Trigger Server of the ϕ -view (TS ϕ) looks at all segments transmitted by the TRACOs and selects the two best segments in the chamber. However, different trigger configurations are possible; the trigger choice will be discussed in the following Section 3.3. The BTI, TRACO and TS ϕ chips are mounted together with the read-out electronics on the minicrate, which is visible in Figure 3.7.

3.2.2 Silicon Detectors

Silicon telescopes constitute, together with the Muon Chamber, the tracking system of the experiment. They are different for dimensions and pitch. Some of them are shown in Figure 3.8.

- Si10 and Si20: they are two double side Silicon layers with 384 strips per side; the surface measures $1.92 \times 1.92 \text{ cm}^2$ and thickness $300 \mu\text{m}$; the pitch is $50 \mu\text{m}$ large.

- Si30: it is made of two double side Silicon layers (one side read in each of them), with 384 strips per side; each of them has a surface of $1.92 \times 1.92 \text{ cm}^2$ and is $300 \mu\text{m}$ thick, while the pitch measures $50 \mu\text{m}$.
- Si40: it is made of two single side Silicon layers with 384 strips per side; each of them measures $9.5 \times 9.5 \text{ cm}^2$ at the surface and is $410 \mu\text{m}$ thick. The pitch is $242 \mu\text{m}$ large.
- Si50, Si51, Si55 and Si56: each of them is made of two single side Silicon layers with 384 strips per side, the surface measures $8.75 \times 8.75 \text{ cm}^2$, thickness $400 \mu\text{m}$ and pitch $228 \mu\text{m}$.

3.2.3 Calorimeters

Different types of calorimeters have been included in the experimental setup. Figure 3.9 shows the disposition of calorimeters in the experimental area.

DEVA Calorimeter It is an electromagnetic calorimeter and it is used to identify a $\mu^+\mu^-$ signal event from the background exploiting the fact that, unlike electrons and positrons, muons do not generate a shower in the calorimeter itself. DEVA, whose insight is visible in Figure 3.5, is a sampling calorimeter composed of 12 plastic scintillator tiles interleaved with 11 lead tiles (eight tiles 0.5 cm thick and three 1 cm thick) for a total of about $13X_0$. Each plastic scintillator tile measures $15 \times 15 \times 2 \text{ cm}^3$. The light is carried by wave-length shifter fibers to a photomultiplier tube.



Figure 3.5: The DEVA calorimeter from the top (without cover).

PbWO₄ Calorimeter It is a component of the CMS experiment's electromagnetic calorimeter: it was meant to measure $e^+e^- \rightarrow \gamma\gamma$ events in order to normalize the muon rate production, as explained in Section 2.2. But due to circumstantial reasons, mostly the short time accorded to the test beam, this measure could not be taken. Normalization will be provided by Bhabha scattering measurements.

Pb glass Calorimeter It is a homogeneous calorimeter from OPAL experiment: it is made of a $11.5 \times 11.5 \times 40 \text{ cm}^3$ lead glass bar read by a photomultiplier.

Cherenkov Calorimeter It is made of two layers of square-based Cherenkov bars with a 50 cm-thick iron block; Cherenkov light is read by four photomultipliers, two per layer. Together with the Pb glass calorimeter it has been positioned in the μ^- line to provide a discrimination between muons and electrons passing through the Muon Chamber.

3.2.4 Scintillator Detectors

The experimental layout included 4 plastic scintillator detectors, whose sizes match those of the Silicon detectors. In fact they have been positioned just after the first two and the last two Silicon detectors' stations, as shown in the experimental layout, Figure 3.2. This choice is motivated by triggering reasons, discussed in the following Section 3.3.

3.3 Trigger and data acquisition

Data acquisition in LEMMA test beam has been carried out with two VME crates positioned in the same rack: one dedicated to the Muon Chamber, the other to all the other detectors. The integration of information coming from all the detectors is done offline, as described in Section 4.4.

During the test beam different trigger configurations have been tried.

Muon Chamber & S1 The trigger signal is generated by the Muon Chamber; the coincidence with the scintillator detector is added in order to avoid triggering in correspondence with cosmic rays. The signal is then sent to the Silicon detectors, that return a busy signal, as illustrated in Figure 3.6: the dead time of the busy state (corresponding to the time needed to write Silicon detectors buffer), amounts to 0.5 ms, which does not represent a problem considering the trigger rate expected (see Section 3.1).

Since the beginning of the test beam, a problem has been noticed: a huge electromagnetic noise on the Muon Chamber due to SPS beam extraction towards North Area. In Figure 3.11 it is highlighted in SPS Page One the precise moment when this phenomenon occurred. The noise

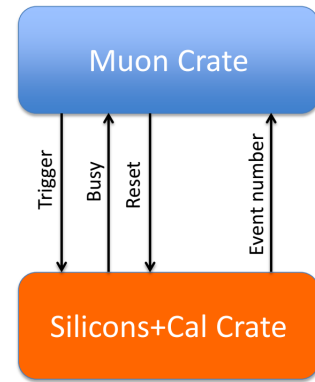


Figure 3.6: Communication scheme between the crate dedicated to the muon chamber and the one dedicated to Silicon detectors and Calorimeters.

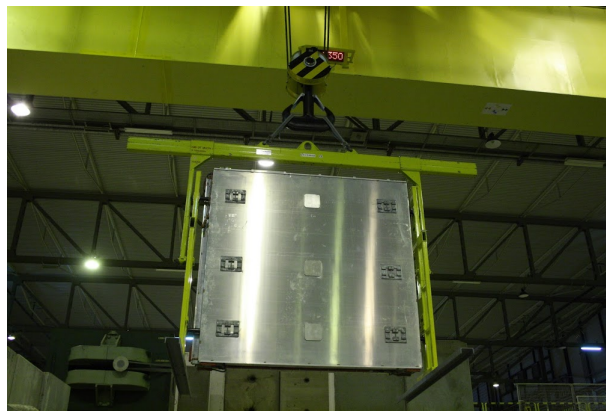
was present even when no beam was delivered to North Area, and it made the trigger rate increase up to 40 kHz, which was unexpected accordingly to the predicted muon production rate. This fact had ripercussions on data acquisition: the Muon Chamber self-trigger and DAQ setup couldn't face this huge amount of data, as evidenced by the fact that the minicrate was often automatically switched off (due to the lack of power needed to process such a volume of data).

Muon Chamber & S1 & DEVA In order to fix this problem, other trigger configurations have been tried: in particular, a coincidence with DEVA calorimeter has been added. In fact with this calorimeter it is possible to easily distinguish electrons and positrons from MIPs according to the signal pulse height, as shown in Section 4.2 Figure 4.11. However, neither this configuration has been able to reduce the huge electromagnetic noise on the Muon Chamber.

S1 & S2 & S4 The Muon Chamber self-triggering system was not reliable: environmental boundary conditions were too unsuitable for the test beam requirements. Moreover, a fault in the initial DAQ setup was found: the busy signal from Silicon detectors to the Muon Chamber was sent with a certain delay. So the decision to proceed on data taking with an external trigger was taken, in particular a triple coincidence of scintillator detectors. The triggering scintillators in the experimental setup are: S1, positioned before the first Silicon telescope Si10, is the first detector that the incoming beam encounters; S2 and S4, positioned after the last Silicon telescopes Si55 and Si56, intercept particles produced in pair.



(a) Details of the minicrate.



(b) Muon Chamber positioning operations.



(c) Muon Chamber behind the iron absorber.

Figure 3.7: Pictures of the Muon Chamber in the experimental area: (a) details of the minicrate, with the Muon Chamber still in horizontal position, (b) the transportation with the bridge crane, (c) the position in the final setup.



Figure 3.8: Some of the Silicon detectors housed in their aluminium boxes in their final position: (a) Si10, the first Silicon detector just outside the beam pipe, (b) Si50 and Si51, the first two Silicon detectors after the magnetic dipole.



Figure 3.9: (a) A picture of DEVA and PbWO₄ calorimeters, positioned in front of the iron absorber. Between them, other iron blocks have been added. (b) A picture of the Pb Glass and Cherenkov calorimeters, placed behind the Muon Chamber.

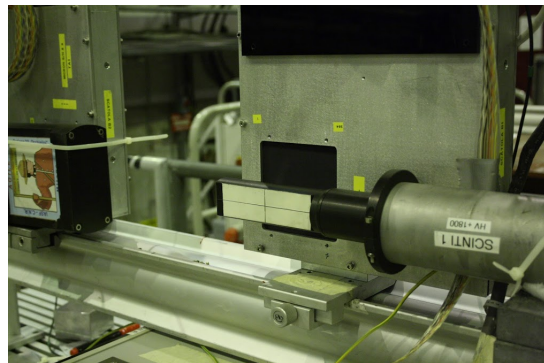


Figure 3.10: S4, the scintillator detector positioned in front of Si56, the last Silicon detector on the μ^+ line before the Muon Chamber.

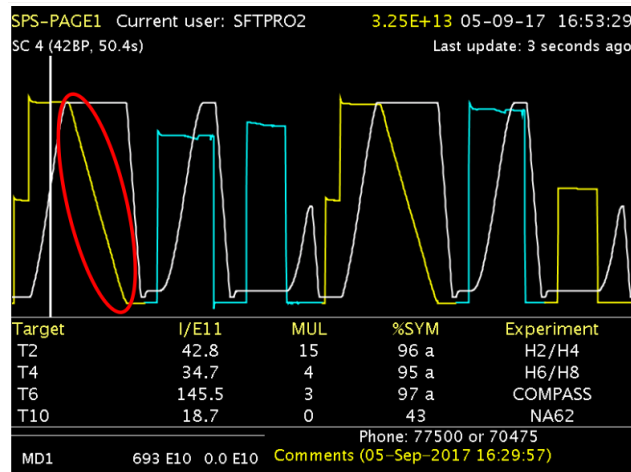


Figure 3.11: A screenshot of SPS Page One: the extraction of the beam from SPS towards North Area that caused a huge electromagnetic noise on the Muon Chamber is highlighted with the red circle.

Chapter 4

Data Analysis and First Results

In this Chapter preliminary results of LEMMA test beam data analysis are illustrated, as well as the future strategies. Alignments of the Silicon detectors, correlation of calorimeters measurements and Muon Chamber performances are discussed respectively in Sections 4.1, 4.2 and 4.3: finally the integration of information from all the detectors and the event tagging approach are presented in Section 4.4. Data used to make these studies come from different runs, whose characteristics are illustrated in Tables A.1, A.2, A.3, A.4 and A.5.

4.1 Tracking system: Silicon telescopes

Silicon telescopes are part of the **tracking system** of the test beam. Their resolution, efficiency and acceptance are thus fundamental issues to be studied; in this Section, alignments and relative positioning are discussed, using data from calibration runs 4606 and 4607. The strategy followed is to study the correlation among hits position in the local reference frame.

Silicon detectors can also be exploited to obtain other kind of information, such as the beam spread.

Alignment of Si20 To easily obtain the correlation between hit positions, both in x-view and y-view, only one-hit events in Si10 and Si20 have been selected. The same cut has been imposed also when studying other couples of Silicon detectors. Results are shown in Figure 4.1, as well as the relative shift between hits coordinates. The correlation between x coordinates is evident; the plot also points out a misalignment of these two detectors, confirmed by the relative shift distribution to be ~ 0.5 cm large. The y coordinate instead shows a negligible relative shift, but the correlation trend suggests that a tilt between these detectors could have been present.

Alignemnt of Si30 The correlation studies shown in Figure 4.2 demonstrate that Si30 has a ~ 1 cm shift in x coordinate with respect to Si10, so, based on the previous result, it must be shifted of ~ 0.5 cm with respect to Si20: as expected, Figure 4.3 shows that the relative shift distribution is peaked around 0.5 cm: furthermore, the distribution looks particularly sharp due to the short distance between Si20 and Si30. In the y coordinate, detector Si30 is ~ 1 cm misaligned both with Si10 and Si20. This of course has a negative consequence in the geometrical acceptance of the first three detectors in the beam line direction, that is reduced to 1/4.

Alignemnt of Si40 Si40 is the last detector before the magnetic dipole and is the bigger Silicon telescope in the beam line (see 3.2.2). Figures 4.4, 4.5 and 4.6 show good correlation between x and y coordinates; relative shifts are visible also in this case but the larger dimensions compensate in geometrical acceptance.

Silicon detectors after the magnetic field These detectors are positioned after the magnetic dipole, two in the μ^- line (Si50 and Si55) and two in the μ^+ line (Si51 and Si56), accordingly to Figure 3.2. Correlation of hits position has been studied with 22 GeV calibration runs: the alignments will be studied by extrapolating the DT tracks to the positions of these detectors.

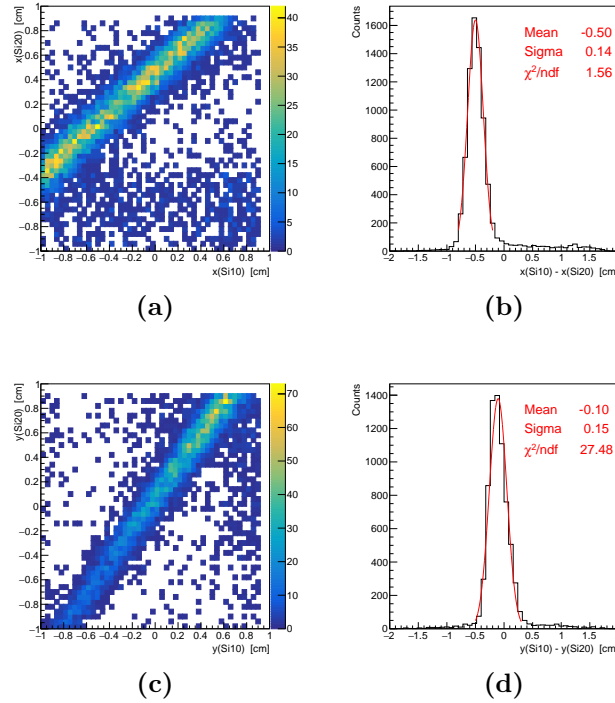


Figure 4.1: Correlation between x coordinates (a) and y coordinates (c) of one-hit events in Si10 and Si20. Difference between x coordinates (b) and y coordinates (d) in the same events.

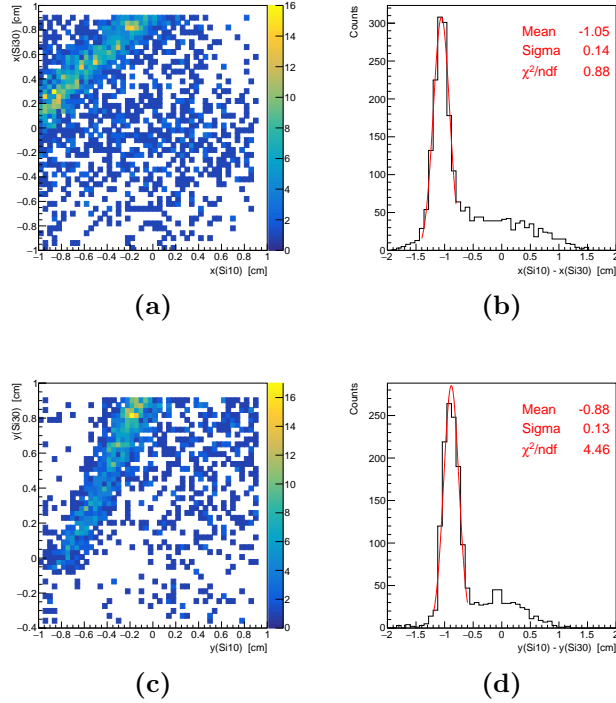


Figure 4.2: Correlation between x coordinates (a) and y coordinates (c) of one-hit events in Si10 and Si30. Difference between x coordinates (b) and y coordinates (d) in the same events.

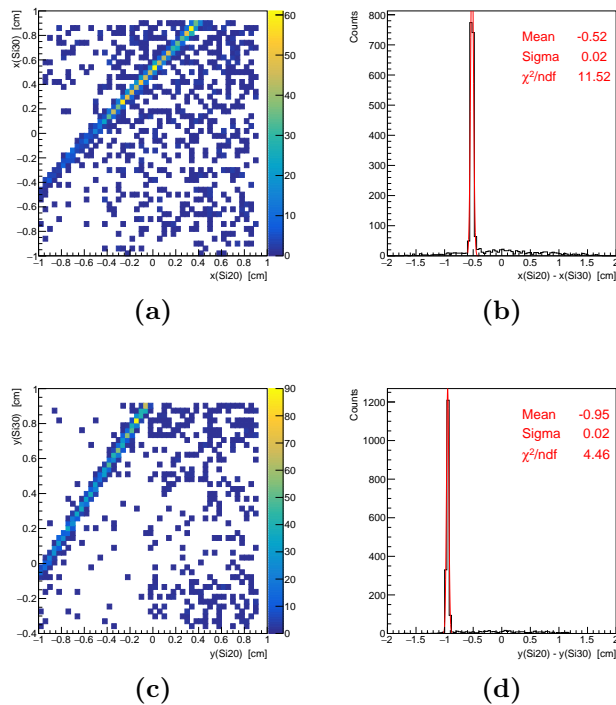


Figure 4.3: Correlation between x coordinates (a) and y coordinates (c) of one-hit events in Si20 and Si30. Difference between x coordinates (b) and y coordinates (d) in the same events.

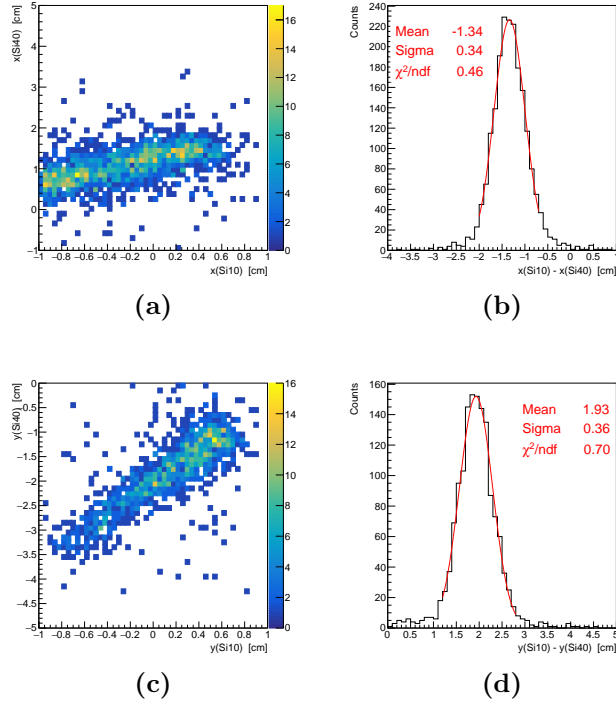


Figure 4.4: Correlation between x coordinates (a) and y coordinates (c) of one-hit events in Si10 and Si40. Difference between x coordinates (b) and y coordinates (d) in the same events.

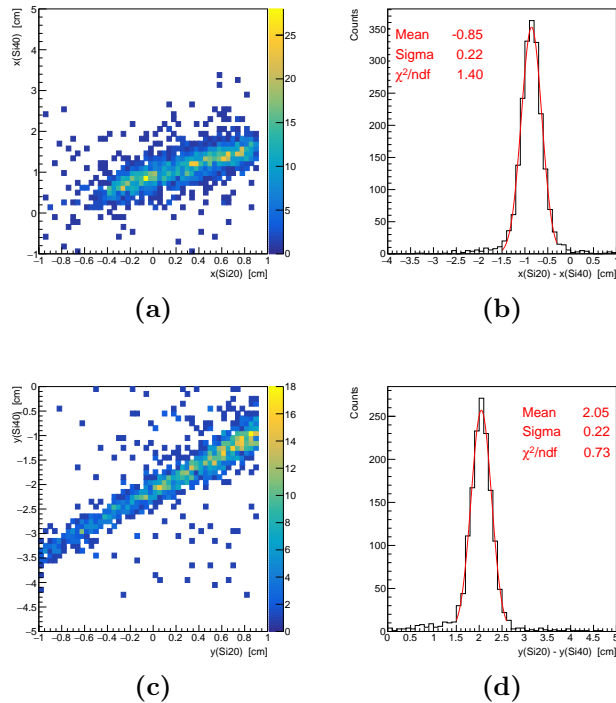


Figure 4.5: Correlation between x coordinates (a) and y coordinates (c) of one-hit events in Si20 and Si40. Difference between x coordinates (b) and y coordinates (d) in the same events.

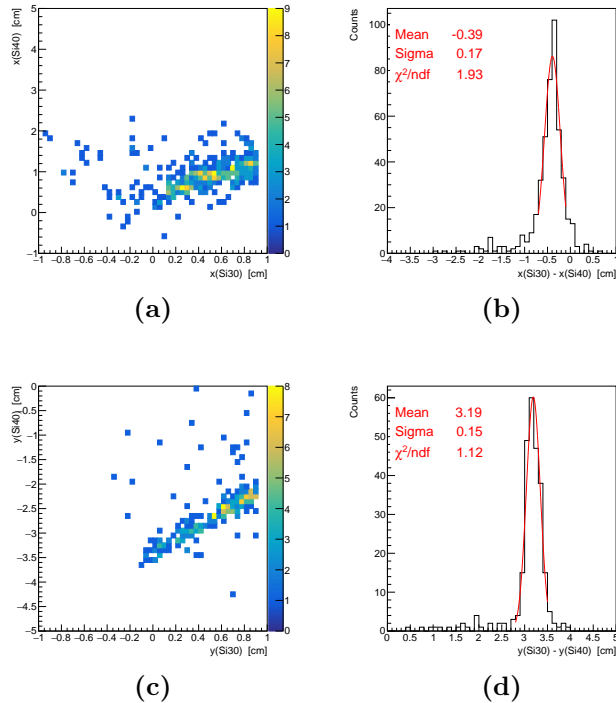


Figure 4.6: Correlation between x coordinates (a) and y coordinates (c) of one-hit events in Si30 and Si40. Difference between x coordinates (b) and y coordinates (d) in the same events.

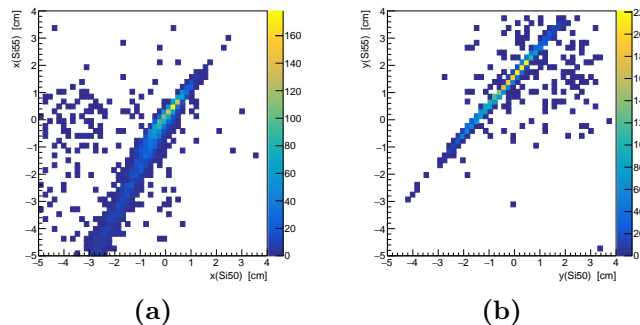


Figure 4.7: Correlation between x coordinates (a) and y coordinates (b) of one-hit events in Si50 and Si55.

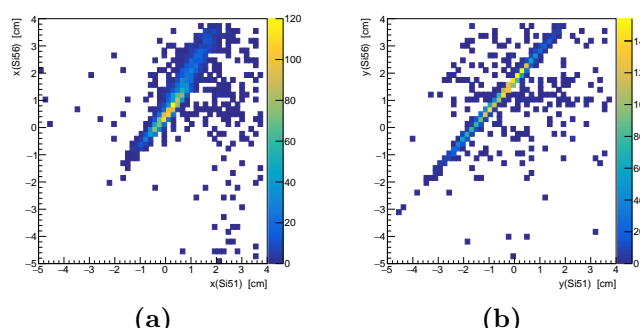


Figure 4.8: Correlation between x coordinates (a) and y coordinates (b) of one-hit events in Si51 and Si56.

4.2 Calorimetry

A powerful tool for **particle identification** at LEMMA test beam is the calorimetry. For this purpose, a set of three calorimeters, described in 3.2.3, has been exploited. The following 4.2.1 and 4.2.2 are dedicated to the performances of these detectors, while in 4.2.3 the correlations among them are thoroughly explored. For tagging purpose, calibration is not needed in a first approach, but a discrimination of MIPs signal from e signals is the only requirement.

4.2.1 Calorimeters on the μ^- line

Two calorimeters are positioned behind the Muon Chamber, as shown in Figure 3.2: a homogeneous Pb glass calorimeter and the Cherenkov calorimeter, described in 3.2.3.

Figure 4.9 illustrates the typical energy spectrum visible with the Pb glass calorimeter: the peak at low energy scale is attributable to Minimum Ionizing Particles, (possible **muon candidates**), while the curve at high energy scale is attributable to possible **Bhabha electrons candidates**.

The Cherenkov calorimeter's energy spectrum is shown in Figure 4.10, separately for the forward channels and the backward channels. The front spectrum is very similar to the one of the Pb glass calorimeter, while the back spectrum is more peaked at low energies, because of the thick iron absorber interposed between front and back Cherenkov bars: in fact, this absorber inside the calorimeter is meant to stop electrons and let MIPs pass.

4.2.2 Calorimeters on the μ^+ line

On the μ^+ line, only the sampling calorimeter DEVA has been used (see 3.2.3): a typical spectrum of this calorimeter is shown in Figure 4.11 for all the channels, while Figure 4.11(f) presents the sum of the pulse heights in the six channels. In the spectra, a clear separation between the MIPs region and the positron region is visible, both in the single channel plots and in the global plot. In the last channels a shoulder close to the MIPs peak indicates some 45 GeV beam positrons that enter the calorimeter.

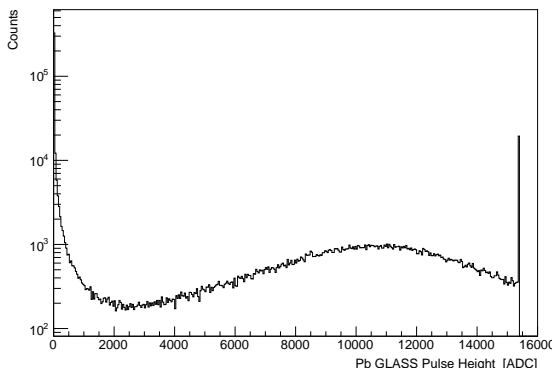


Figure 4.9: The spectrum measured by the Pb glass calorimeter for run 4611.

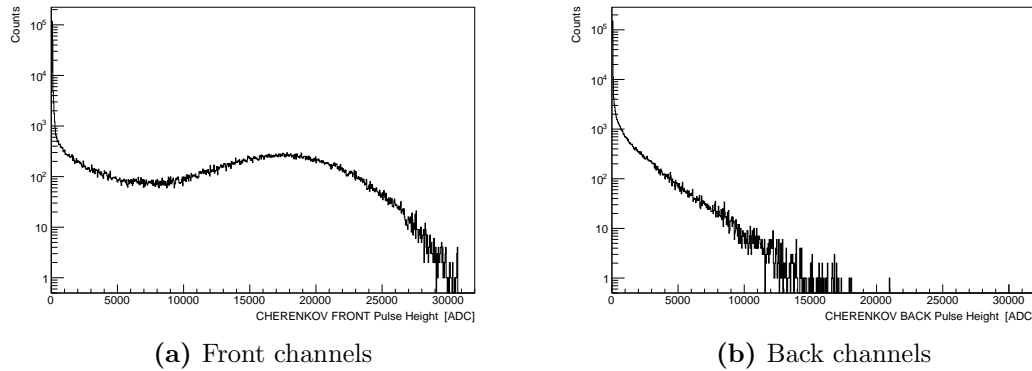


Figure 4.10: The spectrum measured by the Cherenkov calorimeter for run 4611, in the front channels and in the back channels.

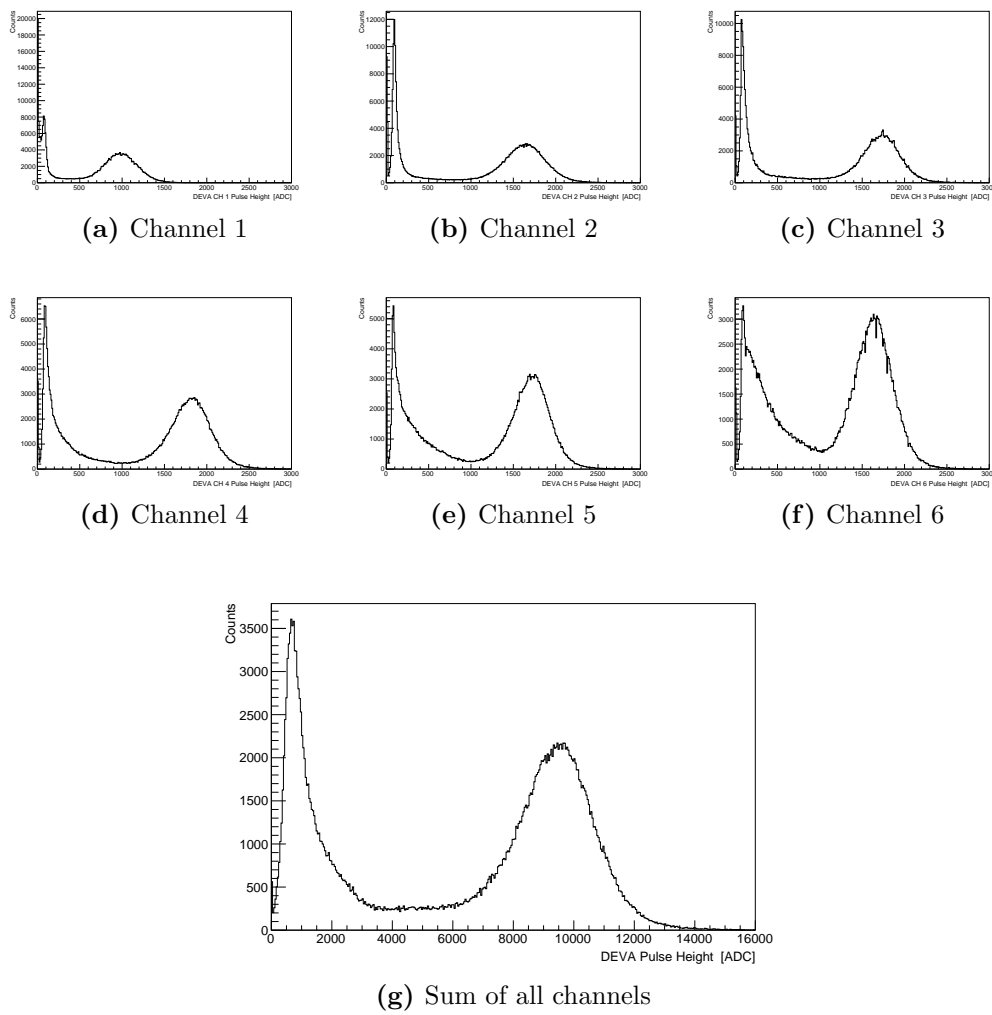


Figure 4.11: The spectrum measured by DEVA in all the six channels for run 4611: the first peak corresponds to the MIPs region, while the last peak corresponds to the positrons region. Plot (g) represents the distribution of the sum of the pulse heights in the six channels.

4.2.3 Correlation studies in calorimeters

In a first step, the correlation between the Pb glass and the Cherenkov calorimeters, i.e. the μ^- line calorimeters has been studied. From the pulse height correlation plots shown in Figure 4.12, 4.13 and 4.14, two main regions can be individuated and associated to MIPs (low energy) and electron signals (high energy).

A simple test of the correlation between Pb glass and Cherenkov calorimeters can be done selecting MIPs and electrons events with Cherenkov calorimeter and checking if the correspondent event in Pb glass is a MIP or an electron signal. The result is reported in Figure 4.15, where it is possible to see that a preliminary event discrimination can be achieved.

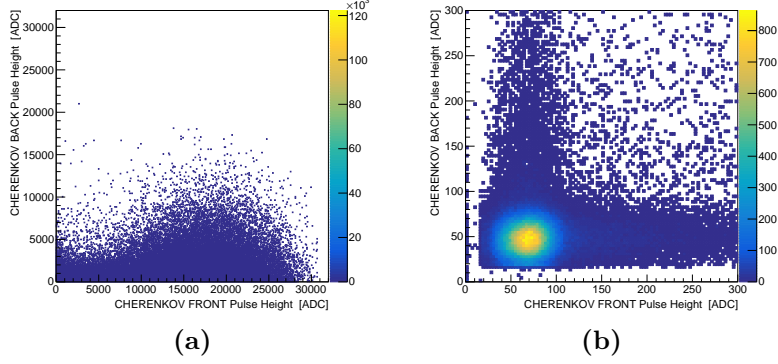


Figure 4.12: Correlation of pulse heights between the front and back channels of Cherenkov calorimeter for run 4611. In (b) the detail of the low energy peak, corresponding to MIP candidates.

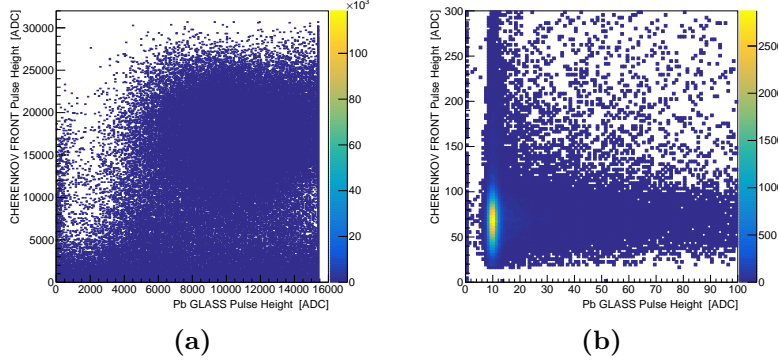


Figure 4.13: Pulse height correlation between the Pb glass and the Cherenkov (front) calorimeter for run 4611. In (b) the detail of the low energy peak, corresponding to MIP candidates.

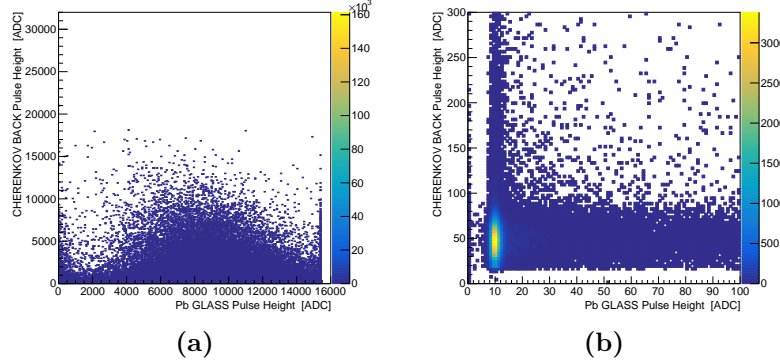


Figure 4.14: Pulse height correlation between the Pb glass and the Cherenkov (back) calorimeter for run 4611. In (b) the detail of the low energy peak, corresponding to MIP candidates.

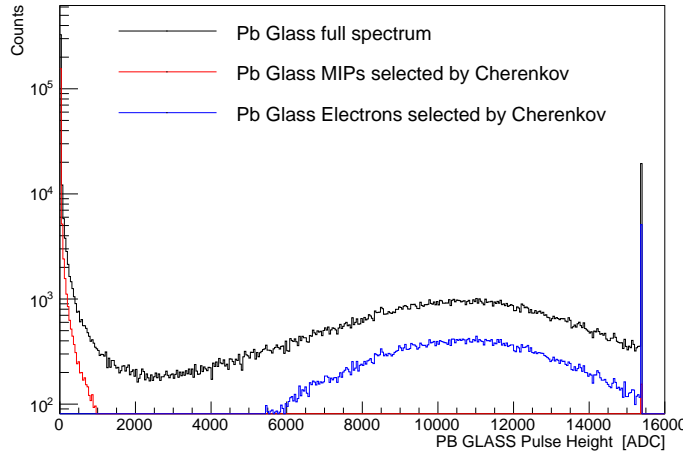


Figure 4.15: Pb Glass events in run 4611 corresponding to those events recognized in Cherenkov calorimeter as MIPs (front PH < 150 ADC and back PH < 100 ADC) and electrons (front PH > 7000 ADC).

In a second step, the correlation between the μ^- line calorimeters and DEVA, in the μ^+ line, has been investigated. The plots in Figures 4.16, 4.17 and 4.18 show the correlation in pulse height of these detectors: it is possible to identify the two interesting regions, one associated to MIPs at low energies and one associated to Bhabha electrons at high energies.

To test the correlation between the μ^- line and the μ^+ line calorimeters the procedure is similar to the previous case: MIPs events are selected with DEVA and Cherenkov, while electrons events are selected with the Cherenkov calorimeter. The result is reported in Figure 4.19: with respect to Figure 4.15 a better discrimination of MIPs event can be achieved exploiting the information from DEVA.

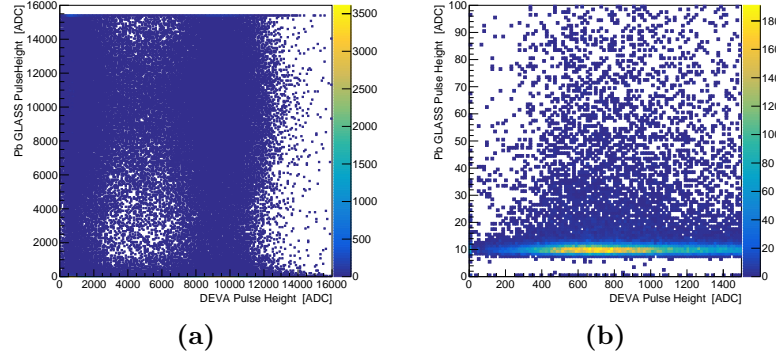


Figure 4.16: Pulse height correlation between the Pb Glass and DEVA calorimeters for run 4611: for DEVA calorimeter the sum of all channels pulse height has been used. In (b) the detail of the low energy peak, corresponding to MIP candidates.

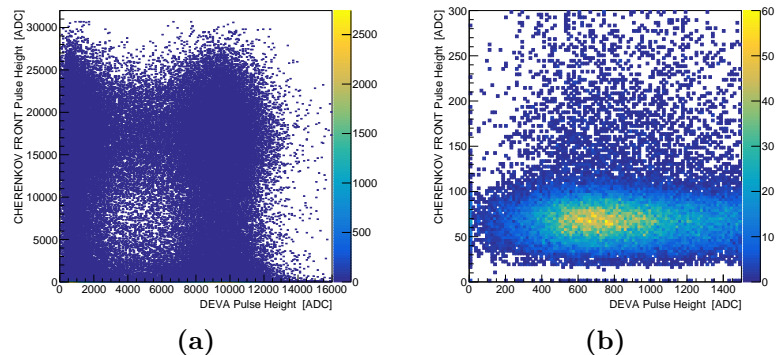


Figure 4.17: Pulse height correlation between the Cherenkov (front channels) and DEVA calorimeters for run 4611: for DEVA calorimeter the sum of all channels pulse height has been used. In (b) the detail of the low energy peak, corresponding to MIP candidates.

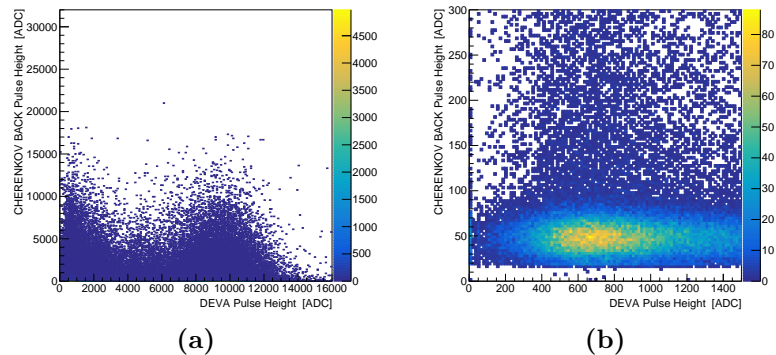


Figure 4.18: Pulse height correlation between the Cherenkov (back channels) and DEVA calorimeters for run 4611: for DEVA calorimeter the sum of all channels pulse height has been used. In (b) the detail of the low energy peak, corresponding to MIP candidates.

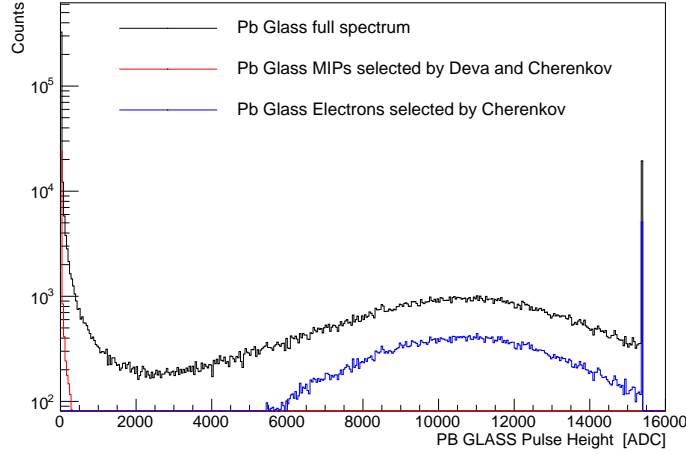


Figure 4.19: Pb Glass events in run 4611 corresponding to those events recognized in Cherenkov and DEVA calorimeters as MIPs (front PH < 150 ADC and back PH < 100 ADC and DEVA PH < 1000 ADC) and electrons (front PH > 7000 ADC).

4.2.4 Energy-position relation in DEVA

Using information from Silicon detectors in the μ^+ line, i.e. Si51 and Si56 (see 3.2) it is possible to associate a position in the xy-plane of DEVA to a momentum and to compare it with a pulse height in DEVA calorimeter. In fact, tracks direction can be reconstructed starting from the hits in Silicon detectors and projected on the surface of DEVA calorimeter: as expected, since the bending in magnetic field depends on the momentum, there is a strong relation between the beam momentum and the final position in DEVA, as shown in Figure 4.20.

Concentrating then on data from calibration run with 22 GeV positrons, events with low pulse height ($50 \text{ ADC} < \text{DEVA ch 1 PH} < 120 \text{ ADC}$) and high pulse height ($\text{DEVA ch 1 PH} > 600 \text{ ADC}$) have been selected: then the correspondent track is reconstructed starting from hits in Si51 and Si56 and projected on DEVA. From this operation, it's possible to understand that the incident beam has some components with lower momentum than the reference value 22 GeV that leave a signal with small pulse height in DEVA calorimeter. The results are shown in Figure 4.21.

The same study has been done with data from run 4611: the result is also shown in Figure 4.21. The low momentum component is present again: so only hits with low pulse height in the 22 GeV region selected with calibration run are safely associable to MIPs.

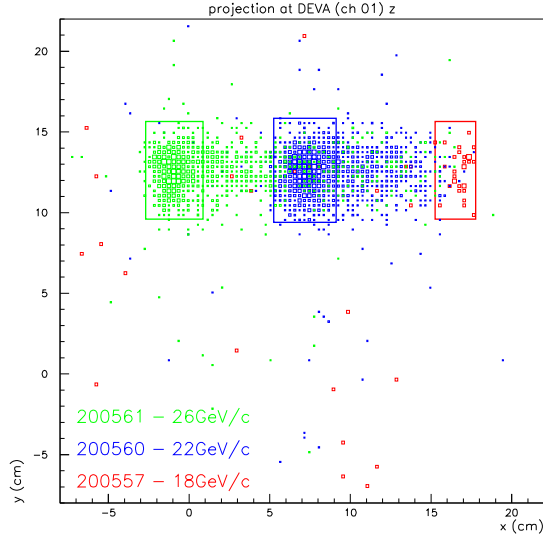


Figure 4.20: Energy and position relation in DEVA calorimeter: red dots are the projection of tracks reconstructed in Si51 and Si56 from 18 GeV calibration run (run 4604), blue dots from 22 GeV calibration run (run 4607), ad green from 26 GeV calibration run (run 4608). *Courtesy of M. Soldani.*

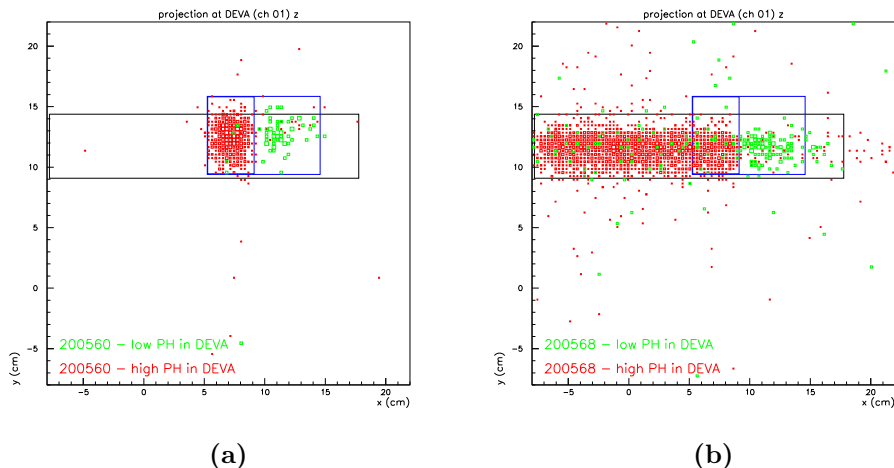


Figure 4.21: Projection of reconstructed Silicon tracks on ch 1 DEVA surface: red dots corresponds to high pulse heights, green dots to small pulse height. In (a) data come from run 4607 (Calibration 22 GeV); in (b) data come from run 4611 (physics run with target), so the momentum continuum is visible. *Courtesy of M. Soldani.*

So in order to exclude the wrong momentum components, the selection of events with DEVA calorimeter can be made with both pulse height and track extrapolation on the surface of this detector. By applying these cuts, DEVA spectra is cleaned especially in the low energy region: the MIPs peak is however visible in the physics run, as shown in Figure 4.22. But if the beam shape along the x direction in the physics run is larger than in the calibration one not only because of the momentum continuum but also because of the bigger beam divergence induced by the presence of the target, then the cut in position on DEVA is too strict and unneeded losses in statistics occur. A study of beam divergence upstream and downstream the target is therefore necessary.

Of course a similar discrimination strategy can be applied also for the μ^- line calorimeters and will be the object of further studies.

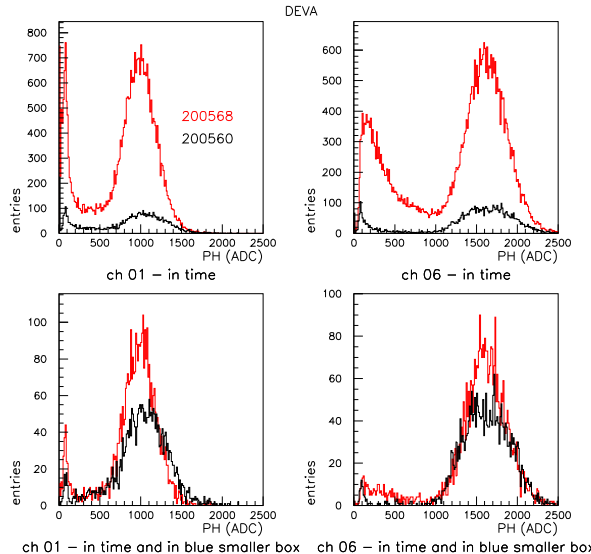


Figure 4.22: Results of energy-and-position-based cuts in calibration run (red) and in physics run (black), on DEVA ch 1 spectrum and DEVA ch 6 (lower figures); events selected are those represented in Figure 4.21 in the small blue box. Results are compared to the all spectrum in ch 1 and in ch 6 (upper figures). *Courtesy of M. Soldani.*

4.3 Muon Chamber performances

The Muon Chamber is dedicated in particular to **muon tracking**: in the following 4.3.1 and 4.3.2 the performances of this detector are analyzed, as long as the track reconstruction algorithm, in 4.3.3.

4.3.1 Time boxes

The time pedestal calibration [14] is the process that allows the extraction of the drift time from the TDC measurements. For an ideal drift cell, the time distribution coming from the TDC (t_{TDC}) would coincide with the distribution of drift time (t_{drift}), and would have a box shape starting from a null drift time, for tracks passing near the anode, up to ~ 380 ns, for tracks passing near the cathode. Experimentally, some non-linear effects related to the electric field distribution inside the drift cell have to be considered in the response of these cells, enhanced by the track inclination. In addition, different time delays, related to trigger latency, and different cable lengths of the read-out electronics also contribute to the TDC measurements. The time measured by the TDC, t_{TDC} , can be expressed as:

$$t_{\text{TDC}} = t_0 + t_{\text{trig}} + t_{\text{drift}} \quad (4.1)$$

being t_0 the inter-channel synchronization used to equalize the response of all channels and t_{trig} the time delay due to the trigger latency. The distribution of t_{TDC} is called “Time Box”. The value of t_{trig} is the turn-on point of the Time Box distribution and it is computed by fitting the rising edge of the distribution.

In Figure 4.23 the Time Box distributions of the three super-layers are shown. With respect to the expected distribution [14], these are very noisy, have a strange wavy shape and present an unexplained shoulder after T_{max} .

The t_{trig} have been calculated separately for the three super-layers and are reported in Table 4.1.

Super-layer	t_{trig} [ns]	$\sigma_{t_{\text{trig}}}$ [ns]
1	3105.15	25.73
2	3097.54	17.14
3	3099.33	17.97

Table 4.1: Muon Chamber t_{trig} results.

4.3.2 Occupancies

In Figure 4.24 the occupancies of the Muon Chamber for each super-layers are shown: the x axis represents the drift cells number. As expected, on the y-view, given by the $\theta - \text{SL}$, hits are concentrated in a small spot while in the x-view, given by the $\phi - \text{SLs}$, hits are spread all over the chamber because of the magnetic bending. Concentrating on the x-view, the portion of the chamber left uncovered by the iron absorber is clearly visible: the amount of hits in that part is higher than in the rest of the detector. In the covered part two peaks are visible, the first one corresponding

to the slot between DEVA and the iron blocks and the second to the slot between the PbWO_4 calorimeter and the same blocks.

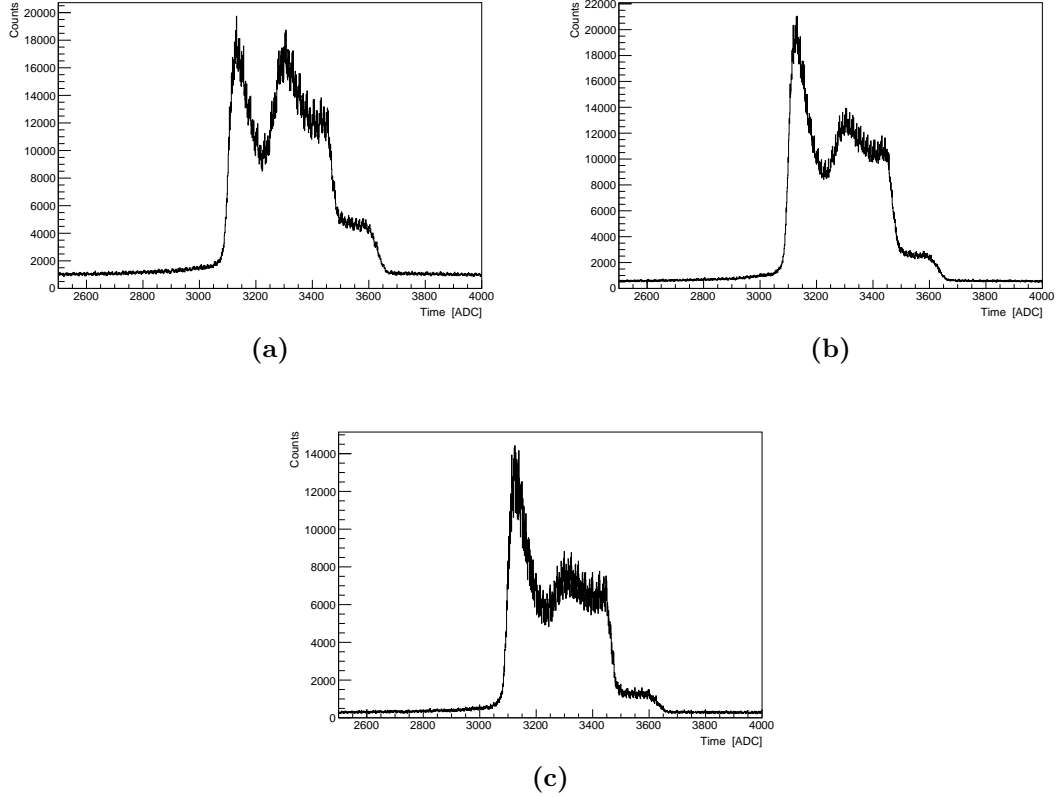


Figure 4.23: Time boxes of the DT chamber in the tree superlayers for run 4611: (a) first $\phi - \text{SL}$, (b) second $\phi - \text{SL}$, (c) $\theta - \text{SL}$.

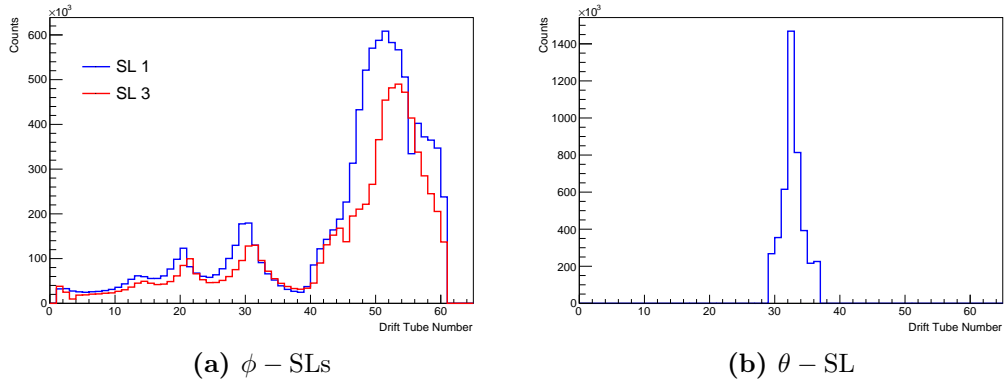


Figure 4.24: Muon Chamber occupancy for run 4611.

4.3.3 Track reconstruction in the Muon Chamber

Pattern recognition and track reconstruction are performed in different steps and separately for the ϕ -SLs and θ -SL: the algorithm is different in its initial part from that used by CMS [15], which is not efficient in the context of this test beam, since the events are much noisier than those of CMS. The track reconstruction strategy is thus the following:

- only hits whose drift time belongs to the Time Box and whose x coordinate is in $[-800, -375]$ mm range for μ^- track fit or in $[375, 800]$ mm for μ^+ track fit are selected;
- events with more than 12 hits in these intervals are discarded;
- At least 6 hits in different layers of ϕ -SLs are required (maximum 8);
- For each hit two points are included in the fit:

$$x_{hit}^+ = x_{wire} + v_{drift} \cdot t_{drift} \quad (4.2)$$

$$x_{hit}^- = x_{wire} - v_{drift} \cdot t_{drift} \quad (4.3)$$

where v_{drift} is considered as a constant all over the cell volume;

- hits are then stored in collections, corresponding to all possible combinations of selected hits in different layers: for each collection a linear fit is performed using the hit positions and errors, solving the left-right ambiguity if possible. A segment candidate is thus built from a set of aligned hits;
- the segment with the maximum number of hits and the minimum $\chi^2/ndof$ is retained, all the others are rejected.
- Segments from ϕ -SLs and θ -SL are associated to form a track. For the test beam, the algorithm has been applied separately for the left side and the right side of the Muon Chamber, since both μ^+ and μ^- tracks are required.

An example of reconstruction (limited to the x view) is given in Figure 4.25, where DT tracks are extrapolated (through a straight line) to the positions of the Si detector after the magnetic field (Si50 and Si55).

Track reconstruction proceeds thus with the following steps: the hit in Si55 nearest to the extrapolated position is selected and a linear fit is performed again using DT track hits and the selected hit in Si55; then track is extrapolated back to Si50 with a straight line and the hit in Si50 nearest to the extrapolated position is selected; after that, a linear fit is performed with DT track hits and the selected hits in Si55 and Si50. With the momentum estimation, extrapolation in Silicon detectors before the magnetic dipole (Si30 and Si40) proceeds with a similar strategy.

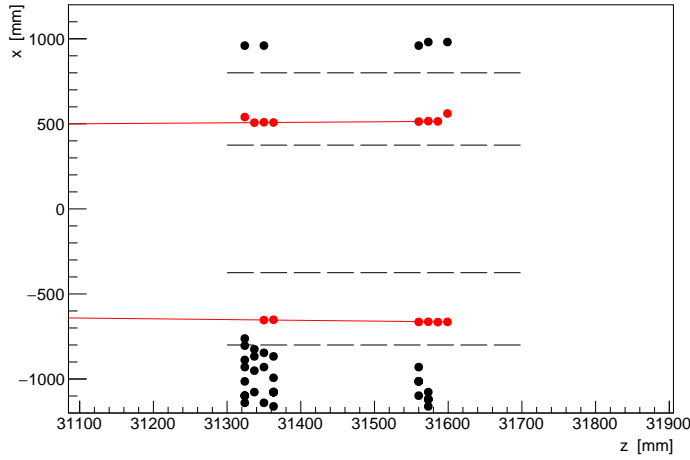


Figure 4.25: Reconstructed tracks of an event in the Muon Chamber: the dashed lines delimit the area where hits are selected for fit. In addition to the fitted points (red), this events contains the usual noise in the μ^- side ($x < 0$) and a third out-of-window track in the μ^+ side ($x > 0$).

4.4 Event building and tagging

Event Building is performed offline: the software matches events from the Muon Chamber and events from Silicon detectors and calorimeters on the basis of the event number, which is assigned accordingly to the scheme in Figure 3.6. There are several conditions that an event must satisfy to be considered a **muon event**:

- Two tracks in the Muon Chamber, in the right windows and with the right slope;
- Pattern reconstruction in the Silicon detectors after the target, requiring the production vertex in the Beryllium target;
- The characteristic MIP signals in the calorimeters;

If instead only one track in the μ^- side is found together with a electromagnetic signal in the calorimeters, that event is considered an **electron event**.

Conclusion

LEMMA test beam ended with a very complicated experimental setup, that evolved during the data taking week to face the various problematic situations that occurred. Even the trigger strategy had to be adapted to the environmental conditions, since the original planned scheme was not suitable for them. In fact the Muon Chamber was too affected by the electromagnetic noise simultaneous to the SPS spill to be reliable. This detector also had to face an unexpected high occupancy, that forced to develop a new event reconstruction software. Furthermore integration tests and alignments with proper calibration beams (muon beams) could not be done, and this brought negative repercussions on the test beam execution.

Anyway good data has been taken: analysis is currently underway, but the first results are promising. Most of all, it has been well understood which aspects must be improved to perform accurate measurements in 2018, when the next test beam will take place:

- Experimental setup. For the tracking system faster devices are needed, while for the muon station the possibility to replace the unique MB2 chamber with multiple smaller DTs is currently under evaluation; furthermore the variety of calorimeters needs to be reduced and rationalized. In general, acceptance and efficiency have to be studied deeply.
- Trigger. A more flexible and redundant trigger strategy has to be implemented.
- Integration test and calibration with proper beams must be realized.
- Software. Both online monitoring and offline software have to be improved.
- More accurate Monte Carlo simulations are needed.

This is the direction where human efforts are now concentrating on.

Appendix A

Characteristics of runs analyzed

The main characteristics of runs analyzed in Chapter 4 are summarized.

Run number:	4604
Silicon run number:	200557
Taken:	1 st August 2017, 05:30 pm
Beam:	Positrons 18 GeV
B generated by:	-437.5 A
Target:	out
Trigger configuration:	Scintillator detector S1

Table A.1: Main characteristics of Run 4604.

Run number:	4606
Silicon run number:	200559
Taken:	1 st August 2017, 06:05 pm
Beam:	Positrons 22 GeV
B generated by:	+437.5 A
Target:	out
Trigger configuration:	Scintillator detector S1

Table A.2: Main characteristics of Run 4606.

Run number:	4607
Silicon run number:	200560
Taken:	1 st August 2017, 06:27 pm
Beam:	Positrons 22 GeV
B generated by:	-437.5 A
Target:	out
Trigger configuration:	Scintillator detector S1

Table A.3: Main characteristics of Run 4607.

Run number:	4608
Silicon run number:	200560
Taken:	1 st August 2017, 06:39 pm
Beam:	Positrons 26 GeV
B generated by:	-437.5 A
Target:	out
Trigger configuration:	Scintillator detector S1

Table A.4: Main characteristics of Run 4608.

Run number:	4611
Silicon run number:	200568
Taken:	2 nd August 2017, 01:00 am
Beam:	Positrons 45 GeV
B generated by:	-437.5 A
Target:	in
Trigger configuration:	Triple coincidence S1·S2·S4
Number of events in muon chamber:	422196

Table A.5: Main characteristics of Run 4611.

Bibliography

- [1] M. Bonesini, “Perspectives for Muon Colliders and Neutrino Factories”, *Frascati Phys.Ser.* 61 (2016) 11-16
[arXiv:1606.00765v1 \[physics.acc-ph\]](https://arxiv.org/abs/1606.00765)
- [2] R. Palmer, “ $\mu^+\mu^-$ Collider, a Feasibility Study”, *BNL-52503* (1996).
- [3] C. Rubbia, “A complete demonstrator of a muon cooled Higgs factory”, *arxiv preprint*
[arXiv:1308.6612v1 \[physics.acc-ph\]](https://arxiv.org/abs/1308.6612v1)
- [4] MICE Collaboration, “Design and expected performance of the MICE demonstration of ionization cooling”, *Phys. Rev. Accel. Beams* 20, 063501 (2017)
[arXiv:1701.06403v2 \[physics.acc-ph\]](https://arxiv.org/abs/1701.06403v2).
- [5] The muon accelerator program.
URL <https://map.fnal.gov>
- [6] M. Boscolo, “Stato studi acceleratore Muon Collider”, *RDFA Collaboration Meeting*, Bologna, 3 July 2017.
- [7] S. Liuzzo, “45 GeV positron ring design”, *8th LEMMA Meeting*, LNF INFN, 25 October 2017.
- [8] M. Antonelli, M. Boscolo, R. Di Nardo, P. Raimondi, “Novel proposal for a low emittance muon beam using positron beam on target”, *Nuclear Instruments and Methods in Physics Research Section A: Accelerators, Spectrometers, Detectors and Associated Equipment* 807 (2016): 101-107.
[arXiv:1509.04454v1 \[physics.acc-ph\]](https://arxiv.org/abs/1509.04454v1)
- [9] S. J. Brodsky, R. F. Lebed, “Production of the smallest QED Atom: True Muonium ($\mu^+\mu^-$)”, *Physical Review Letters* 102.21 (2009): 213401.
[arXiv:0904.2225 \[hep-ph\]](https://arxiv.org/abs/0904.2225)
- [10] M. Zanetti, “Bhabha contribution on the μ^- line”, *LEMMA meeting*, 21 March 2017.

-
- [11] Agostinelli, Sea, et al. “GEANT4—a simulation toolkit”, *Nuclear Instruments and Methods in Physics Research Section A: Accelerators, Spectrometers, Detectors and Associated Equipment* 506.3 (2003): 250-303.
 - [12] GEANT4 Physics List Documentation.
https://geant4.cern.ch/support/proc_mod_catalog/physics_lists
 - [13] CMS Collaboration, “The Muon Project Technical Design Report”, CERN-LHCC-97-032, CMS-TDR-3.
 - [14] CMS Collaboration, “Calibration of the CMS Drift Tube Chambers and Measurement of the Drift Velocity with Cosmic Rays”, CMS PAPER CFT-09-023.
 - [15] CMS Collaboration, “Technical Design Report, Volume I: Detector Performance and Software”, CERN-LHCC-2006-001, CMS-TDR-8-1.